Journal of Computational Physics 229 (2010) 7571–7593

Contents lists available at ScienceDirect

Journal of Computational Physics

journal homepage: www.elsevier.com/locate/jcp

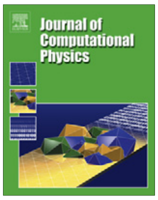

A non-conforming monolithic finite element method for problems of coupled mechanics

D. Nordsletten *, D. Kay, N. Smith

Oxford Computing Laboratory, University of Oxford, UK

ARTICLE INFO

Article history:
Received 19 February 2009
Received in revised form 26 January 2010
Accepted 25 May 2010
Available online 16 June 2010

Keywords:
Finite element method
Mortar/domain decomposition
Navier–Stokes
Arbitrary Lagrangian Eulerian
Finite elasticity mechanics
Non-matching grids

ABSTRACT

In this study, a Lagrange multiplier technique is developed to solve problems of coupled mechanics and is applied to the case of a Newtonian fluid coupled to a quasi-static hyperelastic solid. Based on theoretical developments in [57], an additional Lagrange multiplier is used to weakly impose displacement/velocity continuity as well as equal, but opposite, force. Through this approach, both mesh conformity and kinematic variable interpolation may be selected independently within each mechanical body, allowing for the selection of grid size and interpolation most appropriate for the underlying physics. In addition, the transfer of mechanical energy in the coupled system is proven to be conserved. The fidelity of the technique for coupled fluid–solid mechanics is demonstrated through a series of numerical experiments which examine the construction of the Lagrange multiplier space, stability of the scheme, and show optimal convergence rates. The benefits of non-conformity in multi-physics problems is also highlighted. Finally, the method is applied to a simplified elliptical model of the cardiac left ventricle.

1. Introduction

Coupled mechanical systems are prevalent in a wide-range of disciplines, where conservation principles lay the foundation for multi-physics simulations. Examples in engineering range from aerodynamics [26,25,62,63] through to biomechanics [59,34,69,17]. In these applications, analysis of the underlying physics requires a comprehensive characterization of the mechanical interactions between bodies. As a result, a number of algorithms addressing coupled mechanics problems have been proposed in the literature; falling broadly into three classes (with some exceptions, cf. [20,2]): monolithic, partitioned and immersion.

Monolithic methods, see [30,21,66,39], denote those schemes in which each subproblem is assembled into a single global system. Because of this, monolithic schemes typically rely on equivalent numerical discretizations and methods between bodies. The requirement of equal refinement has the potential to significantly impact either the scheme's computational efficiency (if one body is excessively refined) or accuracy (if one body is under-refined).[1] However, these schemes are generally numerically stable for a wide-range of physical parameters [9,8].

In contrast, partitioned schemes, see [25], are those in which the subproblems are dealt with independently. This approach avoids assembly of a single global system and solves the global system iteratively (in some sense [16,20,26,25]). As a result, these schemes tend to be more computationally efficient than their monolithic counterparts, capitalizing on efficient

---

* Corresponding author. Tel.: +44 1865 282257.
E-mail address: david.nordsletten@gmail.com (D. Nordsletten).

[1] The level of under/over refinement seen is relative to the governing physics and how one chooses to best approximate them.

0021-9991/$ - see front matter © 2010 Elsevier Inc. All rights reserved.
doi:10.1016/j.jcp.2010.05.043

subproblem solution techniques and reduced system size. This efficiency is limited by the stability and accuracy of the method, which is restricted (particularly when the physics of one body do not dominate that governing the other [30]).

Immersion techniques are also commonly used for coupled problems, allowing boundary constraints to be imposed along interfaces which are embedded in a host domain. Two such techniques are the fictitious domain [12,5,27,7,29,61] and immersed boundary [47,48,24,43,67,46,44,71] methods. Both methods are particularly attractive for problems where one body is interior to another (*e.g.* fluid flow through a fiberous network or aortic valve movement [34]). Immersion techniques are well-suited for these problems as they allow complex interfaces as well as dramatic interior movement, avoiding intricate grid construction and adaptation. However, for problems where both bodies are independent or large deformations are experienced on the exterior of a body, these methods can become inefficient (as a larger host domain is required). Further, due to the arbitrary insertion of constraints, the coupling conditions are not smooth [27], weakening the exactness of the coupled solution.

The techniques discussed have advantages and disadvantages, and their appropriate usage is largely application dependent. However, an alternative to these methods can be found in the domain decomposition [4,3,37,18] and mortar domain [11,10] techniques. These methods, developed primarily for parallel implementations on high performance computers, break a single finite element system into a number of subproblems subject to some form of coupling constraint. Using these foundations, we have detailed a linear mechanical theory for coupling using an additional Lagrange Multiplier. Through this approach, the benefits of both monolithic and partitioned schemes (*i.e.* stability and non-conformity) may be effectively combined.

In this paper, we proceed to extend and examine this approach for the case of more complex coupled systems, focusing on the coupling of a Navier–Stokes fluid and a quasi-static hyperelastic solid. Here, we outline the solution procedure, emphasizing the selection of function spaces for the discrete problem. *A priori* stability bounds are shown for the coupled problem, demonstrating the energy preservation of the method. Finally, the method is tested by a series of numerical experiments, showing both convergence and stability for complex non-linear coupled mechanical systems.

1.1. Model problem

In this paper, we focus on the coupling of a Navier–Poisson fluid and a quasi-static hyperelastic solid which satisfy Problems 1 and 2, respectively. Though the paper focuses on these models, the scheme may be generalized to other coupled mechanical systems. The linking of these problems is enforced via Problem 3, ensuring kinematic continuity and equal and opposite traction.

The fluid and solid will be represented geometrically by the domains Ω_1 and Ω_2, respectively. In both cases, $\Omega_i \subset \mathbb{R}^d \times I,\ i = 1,2$ is a moving domain which alters shape through the time interval $I = [0,T]$ (note, $d = \dim\Omega$). The boundary of each domain, Γ_i, is treated to be at least Lipshitz continuous and is partitioned so that $\Gamma_i = \Gamma_i^N \oplus \Gamma_i^D \oplus \Gamma_i^C$ (where N, D, and C refer to the Neumann, Dirichlet and Coupling subdomains of the boundary, respectively). In this case, the two domains are coupled about $\Gamma^C := \Gamma_1^C = \Gamma_2^C$.

Problem 1 (*Navier–Stokes Equations*). Consider flow over Ω_1. Let $\mathbf{v}$ and p be the velocity and pressure state variables, which satisfy,

$$\rho\frac{\partial \mathbf{v}}{\partial t} + \nabla_{\mathbf{x}} \cdot (\rho\mathbf{v}\mathbf{v} - \mu\nabla_{\mathbf{x}}\mathbf{v} + p\mathbf{I}) = \boldsymbol{f}_1 \quad \text{in } \Omega_1, \tag{1a}$$

$$\nabla_{\mathbf{x}} \cdot \mathbf{v} = 0 \quad \text{in } \Omega_1, \tag{1b}$$

$$\mathbf{v} = \boldsymbol{g}_1^D \quad \text{on } \Gamma_1^D, \tag{1c}$$

$$(\mu\nabla_{\mathbf{x}}\mathbf{v} - p\mathbf{I}) \cdot \boldsymbol{n} = \boldsymbol{g}_1^N \quad \text{on } \Gamma_1^N, \tag{1d}$$

$$\mathbf{v}(\cdot, 0) = \mathbf{v}_0 \quad \text{in } \Omega_1(0), \tag{1e}$$

where μ the viscosity, ρ the density, $(\mathbf{I})_{jk} := \delta_{jk}$, n the outward boundary normal, $\mathbf{v}_0$ the initial velocity, $\nabla_{\mathbf{x}}$ the Eulerian gradient operator, f_1 is the contribution to momentum of body forces, and $\boldsymbol{g}_1^D = \boldsymbol{g}_1^D(\mathbf{x}, t)$ and $\boldsymbol{g}_1^N = \boldsymbol{g}_1^N(\mathbf{x}, t)$ the given Dirichlet and Neumann boundary data.

Problem 2 (*Quasi-Static Finite Elasticity*). Consider finite elasticity mechanics over Ω_2. Let $\mathbf{u}$ and φ be the displacement and pressure state variables, which satisfy,

$$-\nabla_{\mathbf{x}} \cdot (\sigma(\mathbf{u}) - \varphi\mathbf{I}) = \boldsymbol{f}_2 \quad \text{in } \Omega_2, \tag{2a}$$

$$\partial_t \mathcal{J}(\mathbf{u}) = 0 \quad \text{in } \Omega_2, \tag{2b}$$

$$\mathbf{u} = \boldsymbol{g}_2^D \quad \text{on } \Gamma_2^D, \tag{2c}$$

$$(\sigma(\mathbf{u}) - \varphi\mathbf{I}) \cdot \boldsymbol{n} = \boldsymbol{g}_2^N \quad \text{on } \Gamma_2^N, \tag{2d}$$

$$\mathbf{u}(\cdot, 0) = \mathbf{u}_0 \quad \text{in } \Omega_2(0), \tag{2e}$$

where ∂_t is the Lagrangian/arbitrary Lagrangian–Eulerian time derivative (refer to Section 3), $\sigma(\mathbf{u}) \in \mathbb{R}^{d\times d}$ is a symmetric stress tensor, $\mathcal{J}(\mathbf{u}) = \det|\nabla_0\mathbf{u}|$ the mapping Jacobian, ∇_0 is the gradient operator with respect to undeformed coordinates, n the outward boundary normal, $\mathbf{u}_0$ the initial displacement, f_2 is the contribution to momentum of body forces, and $\mathbf{g}_2^D = \mathbf{g}_2^D(\mathbf{x},t)$ and $\mathbf{g}_2^N = \mathbf{g}_2^N(\mathbf{x},t)$ the given Dirichlet and Neumann boundary data.

The above problems are common models for detailing fluid flow and solid deformation. Problem 1, the Navier–Stokes system [45,31–33], is the application of Cauchy's first law and mass conservation to a linear, isothermal, incompressible fluid. The so-called arbitrary Lagrangian–Eulerian, or ALE, form of the Navier–Stokes system, a generalization of the governing equations for moving domains, will be used in this work [38,68,53,55,58]. Problem 2 is the quasi-static finite elasticity system [45,13,50,51], governing the displacement of an isothermal, incompressible solid with negligible inertia (relative to that of the fluid). Though the quasi-static solid model was selected – as it is commonly applied for the study of biological tissues [50,51] – transient finite elasticity is not precluded from the presented method.

Problem 3 (*Coupling*). Let $\mathbf{t}_1 = (\mu\nabla_{\mathbf{x}}\mathbf{v} - p\mathbf{I})\cdot n$ and $\mathbf{t}_2 = (\sigma(\mathbf{u}) - \varphi\mathbf{I})\cdot n$, then Ω_1 and Ω_2 are coupled by the following conditions,

$$\mathbf{t}_1 + \mathbf{t}_2 = 0 \quad \text{on } \Gamma^C, \tag{3a}$$

$$\partial_t\mathbf{u} - \mathbf{v} = 0 \quad \text{on } \Gamma^C. \tag{3b}$$

The coupling of subproblems into a single multi-physics system enforces equal, but opposite, traction and kinematic equivalence across the common interface, Γ^C. The force constraint of Eq. (3a) ensures each subproblem provides equal, but opposite, tractions, point-wise at the interface. Further, the kinematic condition of equal velocity, seen in Eq. (3b), subjects each subproblem to a Lagrangian adherence of boundary points (no slip).

The coupled system is assembled through the combination of Problems 1–3. Using standard Galerkin finite elements, this system is reformulated in weak form. As stated, the emphasis of this approach is to allow non-conforming domains while maintaining stability. We note, however, that non-conforming domains invalidate the very premise of Problem 3 as Γ_1^C is not necessarily equal to Γ_2^C or Γ^C. To circumvent these issues, while still maintaining optimality and stability, the constraints of Problem 3 are transformed to a third computational domain, Ξ, and a Lagrange multiplier, λ, is introduced (see Sections 3 and 4).

As we will demonstrate, the mechanical systems given in Problems 1 and 2 may be coupled using an added Lagrange multiplier, resulting in the familiar weak saddle point system shown in Problem 4.

Problem 4 (*Weakly Coupled Fluid–Solid System*). The weakly coupled fluid–solid system may be expressed by the following saddle point problem.

Find $(X,\ Z) \in \mathscr{Y}_{I,D} \times \mathscr{L}_I$ such that,

$$\mathscr{A}_K(X,Y) + \mathscr{B}_K(Z,Y) = F_I(Y) \quad \forall Y \in \mathscr{Y}_{\mathbf{0}}, \tag{4a}$$

$$\mathscr{B}_K(Q,LX) = 0 \quad \forall Q \in \mathscr{L}_I, \tag{4b}$$

where

$$X = (\mathbf{v},\mathbf{u}), \quad Y = (\mathbf{y}_1,\mathbf{y}_2), \quad Z = (p,\varphi,\lambda), \quad Q = (q_1,q_2,\mathbf{q}).$$

$K \subseteq I = [0,T]$, $\mathscr{A}_I$ and $\mathscr{B}_I$ are operators on the kinematic/Lagrange multiplier variables and test spaces, F_I a functional on the test space $\mathscr{Y}_{\mathbf{0}}$, L being the linear operator $LU = (\mathbf{v},\partial_t\mathbf{u})$, and $\mathscr{Y}_I$ and $\mathscr{L}_I$ the appropriate test function spaces.

1.2. Overview

The remainder of this paper is structured as follows. We begin in Section 2 by defining initial terminology and notation. The continuous weak form of both fluid and solid problems is then introduced in Section 3, allowing the natural introduction of the added Lagrange multiplier variable and construction of Problem 4. The system is then discretized and the solution procedure outlined in Section 4. From the linear theory [57], important aspects – both for stability and well-posedness – are noted. In both continuous and discrete systems, *a priori* stability is shown under certain restrictions on the hyperelastic law. Finally, the method is applied to a series of numerical experiments in Section 6, demonstrating its stability and convergence for a range of test problems.

2. Preliminary notation

As we consider the Lagrangian and arbitrary Lagrangian–Eulerian (ALE) reference frames (see Fig. 1) we introduce the following terms and notations. For the transient *physical* domain, Ω, we define a bijective mapping, denoted $\mathcal{P}_\Omega^\Lambda : \overline{\Omega} \to \overline{\Lambda}$, to a static *reference* domain, Λ. The defined mapping then provides a relation between coordinates $\boldsymbol{\eta} \in \Lambda$ and coordinates $\mathbf{x} \in \Omega(\tau)$ for all $\tau \in I$, *i.e.*

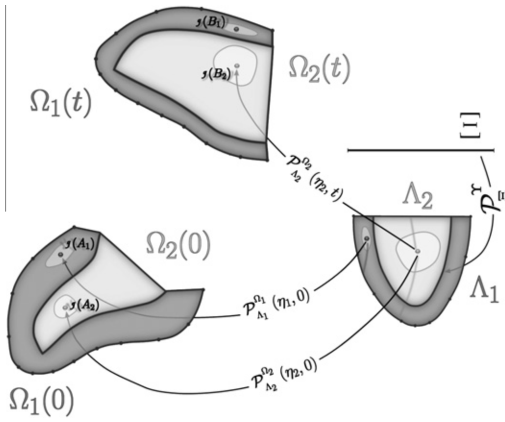

Fig. 1. Example of ALE (light grey, Ω_1) and Lagrangian (dark grey, Ω_2) moving domains at time points 0 and t. Here the reference domains, Λ_1 and Λ_2, are mapped by there respective projections ($\mathcal{P}$). Arrows show the position of points η_1 and η_2 in the reference domain in Ω_1 and Ω_2. Regions around these points are also mapped, showing the relative dilation of volume characterized by the mapping Jacobian, $\mathcal{J}$. The coupling interface, Υ is mapped to the third domain Ξ.

$$\mathcal{P}^{\Lambda}_{\Omega}(\tau) : \overline{\Omega}(\tau) \rightarrow \overline{\Lambda}, \qquad \boldsymbol{\eta} = \mathcal{P}^{\Lambda}_{\Omega}(\mathbf{x},\tau), \quad \forall \mathbf{x} \in \overline{\Omega}(\tau), \ \ \forall \boldsymbol{\eta} \in \overline{\Lambda}, \tag{5}$$

As the mapping is bijective, we may define its inverse, $\mathcal{P}^{\Omega}_{\Lambda}$. Further, $\mathcal{P}^{\Lambda}_{\Omega}$ is defined in so that regions of the physical boundary, Γ, map to regions of the reference boundary, Υ. In this case we think of Ω as the transient Lagrangian or ALE domain and Λ its static reference frame. Using this mapping between the reference and physical domains, a function, $\boldsymbol{f} : \Lambda \rightarrow \mathbb{R}^d$, described on the static reference frame Λ, may be interpreted on Ω as $\hat{\boldsymbol{f}}$,

$$\hat{\boldsymbol{f}}(\mathbf{x},t) := \boldsymbol{f}(\boldsymbol{\eta},t), \qquad \mathbf{x} = \mathcal{P}^{\Omega}_{\Lambda}(\boldsymbol{\eta},t), \quad \forall \boldsymbol{\eta} \in \overline{\Lambda}, \ \ t \in I. \tag{6}$$

The temporal rate-of-change of $\boldsymbol{f}$ on Λ represents the change in the field $\boldsymbol{f}$ along some trajectory in Ω. This time derivative [53,58] can be defined as,

$$\partial_t \boldsymbol{f}(\boldsymbol{\eta},t) := \lim_{|\delta|\rightarrow 0} \frac{\boldsymbol{f}(\boldsymbol{\eta},t+\delta) - \boldsymbol{f}(\boldsymbol{\eta},t)}{\delta}, \quad \boldsymbol{\eta} \in \Lambda, \tag{7}$$

which is related to the Lagrangian (D/Dt) and Eulerian time ($\partial/\partial t$) derivatives by,

$$\frac{D}{Dt}\bar{\boldsymbol{f}} = \frac{\partial}{\partial t}\hat{\boldsymbol{f}} + \mathbf{v} \cdot \nabla_{\mathbf{x}}\hat{\boldsymbol{f}} = \partial_t \boldsymbol{f} + (\mathbf{v} - \mathbf{w}) \cdot \nabla_{\mathbf{x}}\hat{\boldsymbol{f}}, \tag{8}$$

where $\bar{\boldsymbol{f}}$ represents $\boldsymbol{f}$ projected into the Lagrangian frame, $\mathbf{w} = \partial_t \mathcal{P}^{\Omega}_{\Lambda}$ is the domain velocity and $\mathbf{v}$ the Lagrangian frame velocity (equivalent to the fluid/solid material velocity). Note that when the domain velocity is equivalently the Lagrangian frame velocity, ∂_t is simply the Lagrangian time derivative, D/Dt. Similarly, the gradients, $\nabla_{\mathbf{x}}$ and ∇_{η}, on Ω and Λ, respectively, are related by Eq. (9), where $\mathbf{F}_t$ is the deformation gradient tensor of the mapping (at some time $t \in I$),

$$\mathcal{G}_t = \mathbf{F}_t^{-\mathrm{T}}\nabla_{\eta} = \nabla_{\mathbf{x}}, \quad \mathbf{F}_t = \nabla_{\eta}\mathcal{P}^{\Omega}_{\Lambda}(t), \tag{9}$$

so that, the gradient of $\hat{\boldsymbol{f}}$ on Ω is,[2]

$$\nabla_{\mathbf{x}}\hat{\boldsymbol{f}} = \mathcal{G}_t\boldsymbol{f} = \left(\mathbf{F}_t^{-\mathrm{T}}\nabla_{\eta}\right)\boldsymbol{f} = (\nabla_{\eta}\boldsymbol{f})\mathbf{F}_t^{-1}. \tag{10}$$

As the projection of $\boldsymbol{f}$ to $\hat{\boldsymbol{f}}$ may distort the spatial interpretation of $\hat{\boldsymbol{f}}$, the gradients ∇_{η} and $\nabla_{\mathbf{x}}$ are generally not equivalent. Further, as $\nabla_{\mathbf{x}}$ acts on functions on Ω, $\mathcal{G}_t$ is introduced to represent the action of the $\nabla_{\mathbf{x}}$-gradient on functions of Λ. To avoid cluttering notation, the transformation gradient and deformation gradient operators, $\mathcal{G}_t$ and $\mathbf{F}_t$, will not be distinguished between fluid and solid domains – though they will differ, in general – as the appropriate operator and underlying mapping are implicit to each domain.

Lastly, the integral on $\Omega(t)$ at some time t may be detailed on Λ in terms of the weighted integral given by Eq. (11).

$$\int_{\Omega(t)} \hat{\boldsymbol{f}}\,\mathbf{dx} = \int_{\Lambda} \boldsymbol{f}\,\mathcal{J}_{\Omega,t}\,\mathbf{d}\boldsymbol{\eta}, \quad \mathcal{J}_{\Omega,t} = \det|\mathbf{F}_t|. \tag{11}$$

---

[2] For clarity, in this notation we denote the dyadic product of two vectors, **y** and **z**, as **yz**. The tensor components of **yz** are given as $(\mathbf{yz})_{jk} = y_k z_j$.

3. Continuous weak formulation

In this section, the classical Navier–Stokes system, seen in Problem 1, is transformed into its ALE weak form to enable the solution of fluid flow on the dynamic domain, Ω_1. Similarly, the weak form of the quasi-static finite elasticity system, shown in Problem 2, is also derived. Subsequently, a weak formulation of the coupling constraint is derived, using the linear coupled theory developed in [57] to guide formulation construction. Assembling all weak form equations, the coupled system is constructed as shown in Problem 4.

3.1. Problem 1 weak formulation

We begin with the ALE form of the Navier–Stokes equations (refer to [68,49,72,40,55,58] for derivations), a generalization of the classic Navier–Stokes equations to moving domains. In the ALE form, the fluid problem is posed on a static *reference* geometry, Λ_1, which is bijectively related to Ω_1 via the mapping, $\mathcal{P}_{\Lambda_1}^{\Omega_1}$ [53,58] (see Section 2). Derivation of the mapping is done as detailed in [58].

To write the ALE weak form, consider the velocity and pressure, $(\mathbf{v},p)$, on the reference domain, Λ_1. The state variable spaces are defined as [64,65,54],

$$\mathscr{V} := \mathbf{H}^1(\Lambda_1), \quad \mathcal{W}(\Lambda_1) := L^2(\Lambda_1), \tag{12}$$

and

$$\mathscr{V}_I := L^\infty(I;\mathbf{L}^2(\Lambda_1)) \cap L^2(I;\mathbf{H}^1(\Lambda_1)), \quad \mathcal{W}_I(\Lambda_1) := L^\infty(I;L^2(\Lambda_1)). \tag{13}$$

These spaces may be tailored for the weak form solutions to Problem 1 by selecting only those functions which match $\mathbf{g}_1^D$ or 0 on the Dirichlet boundaries, *i.e.*

$$\mathscr{V}_{I,D} = \{\mathbf{y} \in \mathscr{V}_I | \mathbf{y} = \mathbf{g}_1^D \text{ on } \Upsilon_1^D\}, \quad \mathscr{V}_0 = \{\mathbf{y} \in \mathscr{V} | \mathbf{y} = 0 \text{ on } \Upsilon_1^D\}.$$

The weak ALE form of Problem 1 may then be written as: Find $(\mathbf{v},p) \in \mathscr{V}_{I,D} \times \mathcal{W}_I(\Lambda_1)$, such that for any $(\mathbf{y},q) \in \mathscr{V}_{\mathbf{0}} \times \mathcal{W}(\Lambda_1)$ and any $[a,b] \subseteq I$,

$$\begin{aligned}\rho \boldsymbol{m}_b(\mathbf{v},\mathbf{y}) - \rho \boldsymbol{m}_a(\mathbf{v},\mathbf{y}) &+ \rho \int_a^b \mathbf{c}_\tau(\mathbf{v}-\mathbf{w};\mathbf{v},\mathbf{y})\mathrm{d}\tau + \mu \int_a^b \boldsymbol{a}_\tau(\mathbf{v},\mathbf{y})\mathrm{d}\tau \\ &- \int_a^b \boldsymbol{b}_\tau(p,\mathbf{y})\mathrm{d}\tau - \int_a^b \int_{\Upsilon_1^C} \mathbf{t}_1(\tau)\cdot \mathbf{y}\mathcal{J}_{\Gamma_1,\tau}\mathbf{d}\boldsymbol{\eta}\mathrm{d}\tau = \int_a^b \boldsymbol{m}_\tau(\boldsymbol{f}_1,\mathbf{y}),\end{aligned} \tag{14a}$$

$$\int_a^b \boldsymbol{b}_\tau(q,\mathbf{v})\mathrm{d}\tau = 0, \tag{14b}$$

where $\mathbf{t}_1$ is the traction on the coupling interface, $\boldsymbol{f}_1 \in L^2(\mathrm{I};L^2(\Lambda_1))$ represents body forces, and

$$\boldsymbol{m}_\tau(\mathbf{v},\mathbf{y}) := \int_{\Lambda_1} \mathbf{v}(\tau)\cdot \mathbf{y}\mathcal{J}_{\Omega_1,\tau}\mathbf{d}\boldsymbol{\eta}, \tag{15}$$

$$\boldsymbol{a}_\tau(\mathbf{v},\mathbf{y}) := \int_{\Lambda_1} \mathcal{G}_\tau \mathbf{v}(\tau) : \mathcal{G}_\tau \mathbf{y}\mathcal{J}_{\Omega_1,\tau}\mathbf{d}\boldsymbol{\eta}, \tag{16}$$

$$\boldsymbol{b}_\tau(p,\mathbf{y}) := \int_{\Lambda_1} p(\tau)\mathcal{G}_\tau \cdot \mathbf{y}\mathcal{J}_{\Omega_1,\tau}\mathbf{d}\boldsymbol{\eta}, \tag{17}$$

$$\mathbf{c}_\tau(\mathbf{z}-\mathbf{w};\mathbf{v},\mathbf{y}) := \int_{\Lambda_1} \left[\mathcal{G}_\tau \cdot [(\mathbf{z}(\tau)-\mathbf{w}(\tau))\mathbf{v}(\tau)]\cdot \mathbf{y} - \frac{1}{2}(\mathcal{G}_\tau \cdot \mathbf{z}(\tau))\mathbf{v}(\tau)\cdot \mathbf{y}\right]\mathcal{J}_{\Omega_1,\tau}\mathbf{d}\boldsymbol{\eta}, \tag{18}$$

are operators, where $\boldsymbol{m}$ represents the integrated acceleration term, $\boldsymbol{a}$ the linear viscous term, $\boldsymbol{b}$ the pressure term, and $\boldsymbol{c}$ the convective term (where the second component – which is zero in the continuous form – is added for stability [53]). For ease, we have assumed $\boldsymbol{g}_1^N := 0$ in Eq. (14a).

Remark 1. Note, by definition, the test function $\mathbf{y}$ is defined to be constant over time on the reference domain.

3.2. Problem 2 weak formulation

In Problem 2, a solid mechanical system was introduced. Here, we follow the common approach of considering the hyperelastic body in the Lagrangian reference/coordinate frame [13,54]. Similar to the ALE case, reference and physical geometries (denoted Λ_2 and Ω_2, respectively) are defined. Both domains are related by the mapping in Eq. (5) however, in this case $\mathcal{P}_{\Lambda_2}^{\Omega_2}(\tau) := \mathbf{u}(\boldsymbol{\eta},\tau) + \boldsymbol{\eta}$, where $\mathbf{u}$ is the displacement field and $\boldsymbol{\eta}$ a point in Λ_2 (*i.e.* Λ_2 represents the unstressed body). The displacement and pressure, $(\mathbf{u},\varphi)$, of the solid – also considered on the reference domain – are sought in spaces,

$$\mathscr{U} := \mathbf{H}^1(\Lambda_2), \qquad \mathcal{W} := L^2(\Lambda_2), \tag{19}$$

and

$$\mathscr{U}_I := L^\infty(I;\mathbf{H}^1(\Lambda_2)), \quad \mathcal{W}_I(\Lambda_2) := L^\infty(I;L^2(\Lambda_2)). \tag{20}$$

Similarly, these spaces may be tailored for the weak form solutions to Problem 2 by selecting functions which match $\mathbf{g}_2^D$ or $\mathbf{0}$ on the Dirichlet boundaries, *i.e.*

$$\mathscr{U}_{I,D} = \{\mathbf{y} \in \mathscr{V}_I | \mathbf{y} = \mathbf{g}_2^D \text{ on } \Upsilon_2^D\}, \quad \mathscr{U}_{\mathbf{0}} = \{\mathbf{y} \in \mathscr{V} | \mathbf{y} = \mathbf{0} \text{ on } \Upsilon_2^D\}.$$

Remark 2. The solution $\mathbf{u}(\tau)$, at a time $\tau \in I$, satisfies,

$$\mathbf{u}(\tau) \in \mathscr{U}^\star \subset \mathscr{U},$$

where,

$$\mathscr{U}^\star := \{\mathbf{y} \in \mathscr{U} | \mathcal{L}(\boldsymbol{\eta}) = \mathbf{y}(\boldsymbol{\eta}) + \boldsymbol{\eta},\ \boldsymbol{\eta} \in \Lambda_2 \text{ where } \mathcal{L} \text{ is a bijective mapping}\}.$$

The weak form of Problem 2 may then be written as (refer to [45,13,50] for derivations): Find $(\mathbf{u},p) \in \mathscr{U}_{I,D} \times \mathcal{W}_I(\Lambda_2)$, such that for any $(\mathbf{y},q) \in \mathscr{U}_{\mathbf{0}} \times \mathcal{W}(\Lambda_2)$ and $[a,b] \subseteq I$,

$$\int_a^b \hat{\mathbf{s}}_\tau(\mathbf{u},\mathbf{y}) - \boldsymbol{b}_\tau(\varphi,\mathbf{y})\mathrm{d}\tau - \int_a^b \int_{\Upsilon_2^C} \mathbf{t}_2(\tau)\cdot\mathbf{y}\mathcal{J}_{\Gamma_2,\tau}\,\mathbf{d}\boldsymbol{\eta}\,\mathrm{d}\tau = \int_a^b \boldsymbol{m}_\tau(\boldsymbol{f}_2,\mathbf{y})\mathrm{d}\tau, \tag{21a}$$

$$\boldsymbol{m}_b(q,1) - \boldsymbol{m}_a(q,1) = 0, \tag{21b}$$

where $\boldsymbol{m}_\tau(\boldsymbol{f}_2,\mathbf{y}) = \int_{\Omega_2(\tau)} \boldsymbol{f}_2(\tau)\cdot\mathbf{y}\,\mathbf{d}\boldsymbol{\eta}$, $\mathbf{t}_2$ is the traction on the coupling interface, and $\boldsymbol{f}_2 \in L^2(\mathrm{I};L^2(\Lambda_2))$ represents the body forces, $\boldsymbol{b}$ is the operator seen in Eq. (17) set on Λ_2, and

$$\hat{\mathbf{s}}_\tau(\mathbf{u},\mathbf{y}) := \int_{\Lambda_2} \boldsymbol{\sigma}_\tau(\mathbf{u}) : \mathcal{G}_\tau\mathbf{y}\mathcal{J}_{\Omega_2,\tau}\,\mathbf{d}\boldsymbol{\eta}. \tag{22}$$

For ease, we have assumed $\mathbf{g}_2^N := 0$ in Eq. (21a). Eq. (21b), which preserves the mass/incompressibility of the solid body, requires that the integral measure of any L^2-function is equivalent. That is (by selecting $a = 0$ and $b = \tau$),

$$\int_{\Lambda_2} \mathcal{J}_{\Omega_2,\tau} q\,\mathbf{d}\boldsymbol{\eta} = \int_{\Lambda_2} \mathcal{J}_{\Omega_2,0} q\,\mathbf{d}\boldsymbol{\eta}, \quad \forall q \in L^2(\Lambda_2). \tag{23}$$

Assuming the solid law is sufficiently smooth so that $\boldsymbol{\sigma}(\mathbf{u}) : \mathcal{G}_\tau\mathbf{y} \in L^2(\Lambda_2)$ (at almost every point in time),

$$\mathbf{s}_\tau(\mathbf{u},\mathbf{y}) := \int_{\Lambda_2} \boldsymbol{\sigma}_\tau(\mathbf{u}) : \mathcal{G}_\tau\mathbf{y}\,\mathbf{d}\boldsymbol{\eta} = \hat{\mathbf{s}}_\tau(\mathbf{u},\mathbf{y}) \quad \forall \mathbf{y} \in \mathscr{U}, \tag{24}$$

and by the smoothness of $\boldsymbol{f}_2$ (and defining $\boldsymbol{M}_\tau(\boldsymbol{f}_2,\mathbf{y}) = \int_{\Lambda_2} \boldsymbol{f}_2(\tau)\cdot\mathbf{y}\,\mathbf{d}\boldsymbol{\eta}$),

$$\boldsymbol{m}_\tau(\boldsymbol{f}_2,\mathbf{y}) = \boldsymbol{M}_\tau(\boldsymbol{f}_2,\mathbf{y}), \quad \forall \mathbf{y} \in \mathscr{U}. \tag{25}$$

As a result, the weak solid mechanical system of (21) may be recast as: Find $(\mathbf{u},p) \in \mathscr{U}_{I,D} \times \mathcal{W}_I(\Lambda_2)$, such that for any $(\mathbf{y},q) \in \mathscr{U}_{\mathbf{0}} \times \mathcal{W}(\Lambda_2)$ and $[a,b] \subseteq I$,

$$\int_a^b \mathbf{s}_\tau(\mathbf{u},\mathbf{y})\mathrm{d}\tau - \int_a^b \boldsymbol{b}_\tau(\varphi,\mathbf{y})\mathrm{d}\tau - \int_a^b \int_{\Upsilon_2^C} \mathbf{t}_2(\tau)\cdot\mathbf{y}\mathcal{J}_{\Gamma_2,\tau}\,\mathbf{d}\boldsymbol{\eta}\,\mathrm{d}\tau = \int_a^b \boldsymbol{M}_\tau(\boldsymbol{f}_2,\mathbf{y})\mathrm{d}\tau, \tag{26a}$$

$$\boldsymbol{m}_b(q,1) - \boldsymbol{M}_0(q,1) = 0, \tag{26b}$$

where the stress and forcing terms are no longer weighted by the mapping Jacobian (which is, itself, a function $\mathbf{u}$).

3.3. Introduction of the Lagrange multiplier

Along the coupling interface, the traction forces in both fluid and solid problems, denoted $\mathbf{t}_1$ and $\mathbf{t}_2$, arise naturally through integration by parts [32,33]. The result is a duality pairing appearing in the weak formulation along all Neumann-type boundaries. Considering this pairing on the coupled interface, noting Eq. (3a), and summing the weak form Eqs. (14a) and (26a), we may define the added Lagrange multiplier, λ.

$$\boldsymbol{l}_\tau(\lambda,\mathbf{y}_2 - \mathbf{y}_1) := \int_{\Upsilon^C} \lambda(\tau)\cdot(\mathbf{y}_2 - \mathbf{y}_1)\mathbf{d}\boldsymbol{\eta} = \int_{\Upsilon^C} (\mathbf{t}_1(\tau)\cdot\mathbf{y}_1 + \mathbf{t}_2(\tau)\cdot\mathbf{y}_2)\mathcal{J}_\tau\,\mathbf{d}\boldsymbol{\eta},$$

for any test functions, $(\mathbf{y}_1,\mathbf{y}_2) \in \mathscr{V}_{\mathbf{0}} \times \mathscr{U}_{\mathbf{0}}$, where $\tau \in I$. This form suggests that the weighted traction $\lambda(\tau) \in \mathbf{H}^{-1/2}(\Upsilon^C)$, which is consistent with the fact that the tractions are restrictions to the boundary of the normal gradients of $\mathbf{v}$ and $\mathbf{u}$, respectively. Similarly, considering the weak imposition of the kinematic condition (3b), multiplying by a test function $\mathbf{q} \in \mathbf{H}^{-1/2}(\Upsilon^C)$, provides the sensible weak constraint,

$$\boldsymbol{l}_\tau(\mathbf{q}, \partial_t \mathbf{u} - \mathbf{v}) = 0. \tag{27}$$

The substitution of tractions by λ, and the incorporation of the weak kinematic constraint in Eq. (27) introduces an additional saddle point condition. As such, the selection of the test space for λ is subject to the inf–sup, or LBB, condition [42,6,14,15,52], ensuring the uniqueness of λ. Though $\lambda(\tau) \in \mathbf{H}^{-1/2}(\Upsilon^C)$ is a natural space, due to Dirichlet conditions incorporated in $\mathscr{V}_{\mathbf{0}}$ and $\mathscr{U}_{\mathbf{0}}$, this space may contain components in the nullspace (for instance, if $(\Upsilon^C \cap \Upsilon_1^D) \cap (\Upsilon^C \cap \Upsilon_2^D) \neq \emptyset$). However, a space of Lagrange multipliers, denoted $\mathscr{M}$, may be formed by removing the nullspace of $\boldsymbol{l}$ [57], *i.e.*

$$\mathbf{H}^{-1/2}(\Upsilon^C) = \mathscr{M} \oplus \mathscr{N}_{\boldsymbol{l}},$$

where,

$$\mathscr{N}_{\boldsymbol{l}} = \{\mathbf{q} \in \mathbf{H}^{-1/2}(\Upsilon^C) | \quad \boldsymbol{l}(\mathbf{q}, \mathbf{y}_2 - \mathbf{y}_1) = 0, \quad \forall (\mathbf{y}_1, \mathbf{y}_2) \in \mathscr{V}_{\mathbf{0}} \times \mathscr{U}_{\mathbf{0}}\}.$$

With this selection, the introduced saddle point problem can be shown to satisfy the LBB condition [57].

3.4. Coupled system

In the previous sections, the weak form ALE Navier–Stokes equations, quasi-static finite elasticity equations, and coupling conditions were introduced. Combining these results, a global system seen in Problem 4 may be formulated. Identifying the state variables (velocity, displacement, fluid/solid pressure, and the Lagrange multiplier, λ) as either kinematic $X = (\mathbf{v}, \mathbf{u})$ or Lagrange multipliers $Z = (p, \varphi, \lambda)$, we may define the spaces and operators of Problem 4 (where $K = [a, b] \subseteq I$).

$$\mathscr{Y}_{\mathbf{0}} := \mathscr{V}_{\mathbf{0}} \times \mathscr{U}_{\mathbf{0}}, \quad \mathscr{Y}_I := \mathscr{V}_I \times \mathscr{U}_I, \tag{28}$$

$$\mathscr{Z} := \mathcal{W}(\Lambda_1) \times \mathcal{W}(\Lambda_2) \times \mathscr{M}(\Upsilon^C), \quad \mathscr{Z}_I := \mathcal{W}_I(\Lambda_1) \times \mathcal{W}_I(\Lambda_2) \times \mathscr{M}_I(\Upsilon^C), \tag{29}$$

$$\mathscr{A}_K(U, Y) := \rho m_b(\mathbf{v}, \mathbf{y}_1) + \int_K a_\tau(\mathbf{v}, \mathbf{y}_1) + c_\tau(\mathbf{v} - \mathbf{w}; \mathbf{v}, \mathbf{y}_1) + s_\tau(\mathbf{u}, \mathbf{y}_2) d\tau, \tag{30}$$

$$\mathscr{B}_K(Z, Y) := \int_K l_\tau(\lambda, \mathbf{y}_2 - \mathbf{y}_1) - b_\tau(p, \mathbf{y}_1) - b_\tau(\varphi, \mathbf{y}_2) d\tau, \tag{31}$$

$$F_K(Y) := \int_K [m_\tau(f_1, \mathbf{y}_1) + M_\tau(f_2, \mathbf{y}_2)] d\tau + m_a(\mathbf{v}, \mathbf{y}_1). \tag{32}$$

Assembling these definitions, the coupled mechanical system satisfies the fluid, solid and coupling problems introduced in Eqs. (14), (26) and (27).

4. Discrete formulation

The previous section detailed the translation of the classical Problems 1–3 into their weak forms, showing that the coupled system follows the classic saddle point structure of Problem 4. In this section, the discretization of the coupled system is considered using Galerkin finite elements and implicit Euler time stepping. The discrete weak forms are then linearized and broken down into a general block matrix system.

4.1. Discretization

4.1.1. Spatiotemporal discretization

The reference domains, Λ_1 and Λ_2, are split into finitely many, non-overlapping elements, e, which assemble to form the mesh $\mathcal{T}_h(\Lambda_i)$,[3] *i.e.*

$$\mathcal{T}_h(\Lambda_i) = \{e_1, \ldots e_{N_i}\}, \qquad h = \max_{e \in \mathcal{T}_h(\Lambda_i)} diam(e) \quad i = 1, 2.$$

The time domain, I, is also divided into N_I non-overlapping intervals (t^{n-1}, t^n), $t^{n-1} < t^n$, $t^0 = 0$ and $t^N = T$. Over each time interval $t \in (t^{n-1}, t^n]$, the velocity, pressure, Lagrange multiplier and domain velocity are taken as constants in time, while the solid displacement is necessarily piecewise linear in time to satisfy kinematic equality at the coupled interface.

4.1.2. Finite dimensional subspaces

The discretizations $\mathcal{T}_h(\Lambda_1)$ and $\mathcal{T}_h(\Lambda_2)$ provide a foundation for forming finite dimensional polynomial subspaces. Let e_M be a given reference, or master, element and $\mathbb{P}^\kappa(e_M)$ be the polynomial space containing all polynomials of degree[4] no more than κ, $\kappa \geqslant 1$. Then, for every $e \in \mathcal{T}_h(\Lambda_i)$, $i = 1, 2$, we require there be a well-defined bijective, linear or curvilinear map,

---

[3] In this paper, we consider tetrahedral, hexahedral and curvilinear elements.

[4] For tensor product basis, the degree in each direction, while for those basis on triangles or tetrahedra, the total degree (*i.e.* x_1x_2 is degree 2, $x_1^2x_2$ is degree 3, *etc.*).

$$\mathcal{P}^e_{e_M} : e_M \to e, \quad \mathcal{P}^e_{e_M} \in \left[\mathbb{P}^{\kappa_i(\Lambda)}(e_M)\right]^d. \tag{33}$$

where $\kappa_i(\Lambda) \geqslant 1$ is the polynomial degree of the element mapping for Λ_i, and $\mathcal{P}^e_{e_M}$ a map which transforms the master element, e_M, to the mesh element, $e \in \mathcal{T}_h(\Lambda_i)$. With a mapping defined between elements of the mesh and the master element, any set of polynomials on e_M may be projected onto e.

Assembling these locally defined sets of polynomials, a continuous polynomial space, $S^{h,\kappa}(\Lambda_i)$, may be constructed,

$$S^{h,\kappa}(\Lambda_i;\mathcal{T}_h) := \left\{y : \mathcal{T}_h(\Lambda_i) \to \mathbb{R} | y \in \mathcal{C}\left(\mathcal{T}_h(\overline{\Lambda}_i)\right), \quad y|_e \in \mathbb{P}^\kappa(e), \quad \forall e \in \mathcal{T}(\Lambda_i)\right\},$$

which defines all κth-order piecewise-continuous polynomial functions on the mesh elements of $\mathcal{T}_h(\Lambda_i)$. The discrete set, $S^{h,\kappa}$, provides the foundation for constructing the finite dimensional velocity, displacement, and pressure spaces, *i.e.*

$$\mathscr{V}^h := \left[S^{h,\kappa(\mathbf{v})}(\Lambda_1;\mathcal{T}_h)\right]^d, \quad \mathscr{U}^h := \left[S^{h,\kappa(\mathbf{u})}(\Lambda_2;\mathcal{T}_h)\right]^d,$$
$$\mathcal{W}^h(\Lambda_1) := S^{h,\kappa(p)}(\Lambda_1;\mathcal{T}_h), \qquad \mathcal{W}^h(\Lambda_2) := S^{h,\kappa(\varphi)}(\Lambda_2;\mathcal{T}_h),$$

where $\kappa(\mathbf{v})$ is the order of interpolation of the velocity and similarly for the displacement/pressures. Though the power of the kinematic variables is arbitrary, in this paper we use the LBB-stable general Taylor–Hood elements, see [28,15]. Each discrete subspace has finite dimension which is given by,

$$N_v = \operatorname{span}\mathscr{V}^h, \quad N_u = \operatorname{span}\mathscr{U}^h, \quad N_p = \operatorname{span}\mathcal{W}^h(\Lambda_1), \quad N_\varphi = \operatorname{span}\mathcal{W}^h(\Lambda_2).$$

By definition, the dimension of each discrete subspace is related to the underlying nodal Lagrange space. For example, denoting the dimension of $S^{h,\kappa(\mathbf{v})}(\Lambda_1;\mathcal{T}_h)$ as $N_{\kappa(\mathbf{v})}$, the dimension of $\mathscr{V}^h$ is $N_v = d\, N_{\kappa(\mathbf{v})}$ (and similarly for the solid displacement); while in the case of the pressure, $N_p = N_{\kappa(p)}$ (and similarly for the solid pressure). Due to the finite dimension, all of the discrete approximations may be written as a weighted sum of basis functions [60,32,33], denoted ψ and $\boldsymbol{\psi}$ for scalar and vector functions, respectively. Here subscripts will be used to indicate the state variable, and superscripts the basis function. Thus, at any time t^n, $n \in [0,N]$,

$$\mathbf{v}^{h,n} = V^n \cdot \boldsymbol{\Psi}_v, \quad \mathbf{u}^{h,n} = U^n \cdot \boldsymbol{\Psi}_u, \quad p^{h,n} = P^n \cdot \boldsymbol{\Psi}_p, \quad \varphi^{h,n} = \varphi^n \cdot \boldsymbol{\Psi}_\varphi, \tag{34}$$

where

$$\boldsymbol{\Psi}_v = \begin{pmatrix} \boldsymbol{\psi}_v^1 \\ \vdots \\ \boldsymbol{\psi}_v^{N_v} \end{pmatrix}, \quad \boldsymbol{\Psi}_u = \begin{pmatrix} \boldsymbol{\psi}_u^1 \\ \vdots \\ \boldsymbol{\psi}_u^{N_u} \end{pmatrix}, \quad \boldsymbol{\Psi}_p = \begin{pmatrix} \psi_p^1 \\ \vdots \\ \psi_p^{N_p} \end{pmatrix}, \quad \boldsymbol{\Psi}_\varphi = \begin{pmatrix} \psi_\varphi^1 \\ \vdots \\ \psi_\varphi^{N_\varphi} \end{pmatrix}, \tag{35}$$

and, for example, V^n is a constant vector with N_v components (*i.e.* $V^n \in \mathbb{R}^{N_v}$). These weightings – V^n, U^n, *etc.* – are then selected in order to satisfy the *discrete* coupled system.

4.1.3. Finite dimensional Lagrange multiplier subspace

In the fluid–solid system, coupling conditions are weakly upheld on Υ^C. While not significant for the continuous problem, in the discrete setting two problems arise. Due to the variability between mesh size and geometric interpolation (linear versus curvilinear), the domain on the fluid side need not be equivalent to that on the solid side, *i.e.* $\mathcal{T}_h(\Upsilon_1^C)$ and $\mathcal{T}_h(\Upsilon_2^C)$. In order to pose a sensible weak form constraint in this setting, it is clear that some mapping between each approximation of Υ^C must be constructed.

Beyond the complications introduced by the discrete physical interfaces, the use of different meshes and state variable interpolations generally results in different trace spaces on each side (note, in the continuous setting both were $\mathbf{H}^{-1/2}(\Upsilon^C)$, refer to Section 3.3). As stated in Section 3.3, a key component to the existence and uniqueness of λ is the establishment of an inf–sup stable space, $\mathscr{M}$. The ability of this approach to succeed in the discrete setting is then linked to the inf–sup stability of $\boldsymbol{l}$ on $\mathscr{V}_{\mathbf{0}}^h$, $\mathscr{U}_{\mathbf{0}}^h$ and $\mathscr{M}^h$.

To overcome the complications due to different spatial meshes of the coupling boundary, a third domain, $\Xi \subset \mathbb{R}^{d-1}$, is introduced which is bijectively mapped to $\mathcal{T}_h(\Upsilon_1^C)$ and $\mathcal{T}_h(\Upsilon_2^C)$ by $\mathcal{P}_\Xi^{\Upsilon_i^C}$ (see Eq. (5) and Fig. 2). Mapping the constraints to this domain, the Lagrange multiplier, λ, is redefined as the Jacobian weighted traction on Ξ. As a result, the discrete λ^h and operator, $\boldsymbol{l}$, is redefined as,

$$l_\tau(\lambda^h, \mathbf{y}_2^h - \mathbf{y}_1^h) := \int_\Xi \lambda^h(\tau) \cdot (\hat{\mathbf{y}}_2^h - \hat{\mathbf{y}}_1^h)\mathbf{d}\boldsymbol{\xi} = \int_{\Upsilon^C} (\mathbf{t}_1^h(\tau) \cdot \mathbf{y}_1^h + \mathbf{t}_2^h(\tau) \cdot \mathbf{y}_2^h)\mathcal{J}_\tau \mathbf{d}\boldsymbol{\eta},$$

where $\mathbf{t}_1^h$ and $\mathbf{t}_2^h$ are the tractions resulting from the discrete approximations. Note that *hats* are added to $\mathbf{y}_1^h$ and $\mathbf{y}_2^h$ as they must be projected to Ξ by the mapping, *i.e.* following Eq. (36),

$$\hat{\mathbf{y}}_2^h(\boldsymbol{\xi}) := \mathbf{y}_2^h(\boldsymbol{\eta}), \qquad \boldsymbol{\xi} = \mathcal{P}^{\Xi}_{\Upsilon_2^C}(\boldsymbol{\eta}), \quad \forall \boldsymbol{\eta} \in \bar{\Upsilon}_2^C. \tag{36}$$

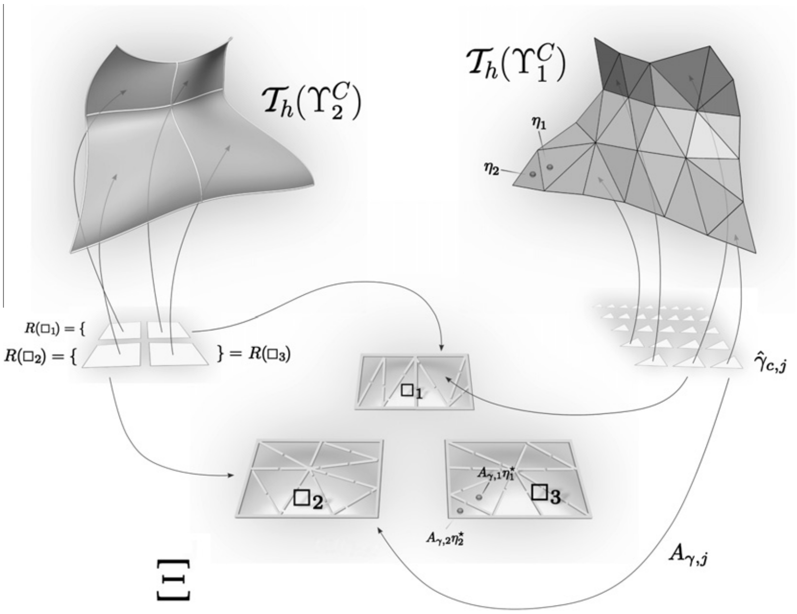

Fig. 2. Shown are the meshes resulting from each approximation of the boundary Υ^C, $\mathcal{T}_h(\Upsilon_1^C)$ and $\mathcal{T}_h(\Upsilon_2^C)$, for a curvilinear hexahedral solid mesh coupled to a tetrahedral fluid mesh. Each surface element in the meshes are defined in relation to a set of simple squares or triangles (which compose boundaries of the master element for each mesh). Denoting the surface element $\gamma_{c,j} \in \mathcal{T}_h(\Upsilon_1^C)$, the corresponding surface in the master element is given as $\hat{\gamma}_{c,j}$ (and similarly for the solid). Defining the fluid mesh nested within the parametric solid mesh, simple affine mappings may be used to define the relationship between these meshes, denoted $A_{\gamma,j}$ for the surface element $\hat{\gamma}_{c,j}$. As the fluid mesh is defined relative to the master element surfaces of the solid mesh, a natural choice for $\{\square_1 \cdots \square_{N_\square}\}$ are simply the master elements themselves; however, this is not essential (as seen for $\square_1$). In this case, three conforming regions are selected – denoted $R(\square_1)$ for $\square_1$, etc. – where $R(\square_1)$ is composed of the top two elements of the solid, while $R(\square_2)$ and $R(\square_3)$ are simply the master surface elements of the solid. Each fluid element is then mapped into these regions, respecting continuity within each region. That is, the affine mapping for two neighboring surfaces, $A_{\gamma,1}$ and $A_{\gamma,2}$, respects the continuity within $\mathcal{T}_h(\Upsilon_1^C)$ (i.e. two points $\boldsymbol{\eta}_1$ and $\boldsymbol{\eta}_2$ near the common edge remain along that edge in $\square_3$ – where $\xi_1 = A_{\gamma,1}\boldsymbol{\eta}_1^\star$, $\xi_2 = A_{\gamma,2}\boldsymbol{\eta}_2^\star$, and $\boldsymbol{\eta}_1^\star$, $\boldsymbol{\eta}_2^\star$ are the corresponding points of $\boldsymbol{\eta}_1$, $\boldsymbol{\eta}_2$ in the master element surface).

The key to executing this computation is the creation of the third domain and the mapping used to relate it to each discrete boundary. In general, the domain boundaries can be complex – as seen in Fig. 2 – leading to non-trivial maps. However, each discrete boundary is a parametric mapping of a surface of the reference element, e_M, see Section 4.1.2. Defining the mapping from these simple shapes, we can use simple linear transformations, denoted A, for each element boundary regardless of the complexity of the mapping between the master element and its shape in the mesh. Such parametric mappings are automatically generated in some tessellation algorithms, such as that of [56], which build surface meshes of another type on a parametric surface mesh.

This choice of mapping shapes the selection of Ξ. A convenient choice for this mapping is selecting $\Xi \in \mathbb{R}^{d-1}$ to be a disjoint set of open regions as seen in Fig. 2, *i.e.*

$$\Xi = \{\square_1 \cdots \square_{N_\square}\}.$$

In this case, $\square_i$ is some region over which the fluid and solid regions overlap. Using the embedding of meshes, a natural choice is for $\square_i$ to be a square or triangle from which the other mesh was derived. More complex selections may be chosen using a collection of elements. This process is detailed in Fig. 2, where a curvilinear hexahedral solid mesh is coupled to a tetrahedral fluid mesh along the coupled boundary.

Focusing now on the construction of $\mathscr{M}^h$, an approximation space for the Lagrange Multiplier, λ^h, must be defined which satisfies the inf–sup condition. This may be accomplished by noting Remark 3.

Remark 3. As the operator, *l*, is linear, inf–sup stability may be guaranteed by selecting $\mathscr{M}^h$ as the set (or subset) of basis functions seen in Ξ from the fluid OR solid [57].

As the Lagrange multiplier is defined on Ξ, a mesh may be easily created (as done for the other state variables). In this case, $\mathcal{T}_h(\Xi)$ is defined by,

$$\mathcal{T}_h(\Xi) = \{\mathcal{T}_h(\square_1), \ldots, \mathcal{T}_h(\square_{N_\square})\}, \qquad \mathcal{T}_h(\square_j) = \left\{\vartheta_{j1}, \ldots, \vartheta_{jM_{\square_j}}\right\}, \quad j = 1, \ldots, N_\square,$$

denote the discretization of each region, $\square \in \Xi$, where $N_\square \leqslant N_\vartheta := \sum_{j=1}^{N_\square} M_{\square_j}$. We note that $\vartheta \in \mathcal{T}_h(\Xi)$ is a triangle or square in $d = 3$, or a line segment in $d = 2$. Following Remark 3, we will choose the tessellation $\mathcal{T}_h(\Xi)$ to be the fluid or solid boundary. In Fig. 2, for example, $\mathcal{T}_h(\Xi)$ may be selected as the set of square elements or set of triangles. $\mathscr{M}^h$ may then be defined as,

$$\mathscr{M}^h = \left\{ \mathbf{z} : \mathcal{T}_h(\Xi) \to \mathbb{R}^d \middle| \mathbf{z} \in \mathscr{C}^*(\mathcal{T}_h(\Xi)), \qquad \mathbf{z}|_\vartheta \in [\mathbb{P}^p(\vartheta)]^d, \quad \forall \vartheta \in \mathcal{T}_h(\Xi) \right\},$$

where

$$\mathscr{C}^*(\mathcal{T}_h(\Xi)) := \left\{ \mathbf{z} : \mathcal{T}_h(\Xi) \to \mathbb{R}^d \middle| \mathbf{z} \in \left[\mathcal{C}\left(\mathcal{P}_{\Xi}^{\Gamma_i^C}(t) \circ \mathcal{T}_h(\bar{\Xi}) \right) \right]^d, \quad \forall i \in [1,2], \ \forall t \in I \right\}.$$

The selection of $\mathscr{M}^h(\Xi)$ based on a *visible* embedding of the fluid or solid trace space (or the trace itself) allows easy construction of the discrete space. Implicit to this construction is that,

$$\kappa(\lambda) \leqslant \max\,[\kappa(\mathbf{v}), \kappa(\mathbf{u})]. \tag{37}$$

In general, we choose $\mathscr{M}^h(\Xi)$ nested inside the richest trace space (though this choice may not always be obvious as it depends on polynomial degree and discretization).

4.1.4. Lagrangian/ALE mapping discretizations

The fluid and solid problems are both set on moving domains (ALE or Lagrangian), which vary with time. In Sections 3.1 and 3.2, domain motion was integrated into the fluid and solid mechanical formulations by introducing a *reference* domain, Λ_i, that may be mapped to the *physical* domain, Ω_i, $i = 1, 2$. The reference to physical mappings are also given by polynomials so that the mapping, at any time t^n, $n \in [0,N]$, satisfies,

$$\mathcal{P}_{\Lambda_i}^{\Omega_i}(t^n) \in \mathscr{K}^{h,\kappa_i(\mathcal{P})}(\Lambda_i;\mathcal{T}_h), \quad \mathscr{K}^{h,\kappa_i(\mathcal{P})}(\Lambda_i;\mathcal{T}_h) := \left[S^{h,\kappa_i(\mathcal{P})}(\Lambda_i;\mathcal{T}_h) \right]^d. \tag{38}$$

We note that, for the fluid $\kappa_1(\Lambda) \leqslant \kappa_1(\mathcal{P})$ and for the solid, $\kappa_2(\mathcal{P}_\Lambda) = \max\,(\kappa_2(\mathcal{P}), \kappa(\mathbf{u}))$.[5] A piecewise continuous interpolation of the mapping is used through time,

$$\mathcal{P}_{\Lambda_i}^{\Omega_i}(\cdot,t) := \frac{t^n - t}{\Delta_t^n} \mathcal{P}_{\Lambda_i}^{\Omega_i}(\cdot,t^{n-1}) + \frac{t - t^{n-1}}{\Delta_t^n} \mathcal{P}_{\Lambda_i}^{\Omega_i}(\cdot,t^n), \quad t \in (t^{n-1},t^n], \ \Delta_t^n = t^n - t^{n-1}, \tag{39}$$

resulting in continuous piecewise linear displacements (for the solid) and piecewise constant domain velocities (for the fluid) through the interval I.

As the fluid and solid systems are coupled about their respective discretizations of Γ^C, the domain movements are inextricably linked. While the solid map is given by the displacement field $\mathbf{u}^h$, the fluid map is arbitrary so long as it adheres to the movement on the coupled boundary. The selection of this map satisfies the weak Laplacian problem [58,54],

$$a_{t^{n-1}}(\mathbf{d}^h, \mathbf{y}^h) = 0, \quad \forall \mathbf{y}^h \in \mathscr{V}_{\mathbf{0}}^h, \tag{40}$$

for $\mathbf{d}^h \in \mathscr{V}^h$ and $\mathbf{d}^h = \Delta_t^n \mathbf{v}^{h,n}$ on Υ_1^C. The ALE mapping is then updated,

$$\mathcal{P}_{\Lambda_1}^{\Omega_1}(t^n) = \mathbf{d}^h + \mathcal{P}_{\Lambda_1}^{\Omega_1}(t^{n-1}),$$

while the solid mapping is updated by the computed displacement $\mathbf{u}^{h,n}$,

$$\mathcal{P}_{\Lambda_2}^{\Omega_2}(t^n) = \mathbf{u}^{h,n} + \mathcal{P}_{\Lambda_2}^{\Omega_2}(t^{n-1}).$$

4.2. Discrete weak form

Following the continuous weak form in Definition 4, and using the discrete conservative ALE Navier–Stokes system (Eqs. (14a) and (14b)) along with the discrete quasi-static finite elasticity system ((26a) and (26b)), the discrete coupled system follows directly from Section 3.4.

Find $(\mathbf{v}^h, \mathbf{u}^h) \in \mathscr{Y}_{I,D}^h, (p^h, \varphi^h, \lambda^h) \in \mathscr{Z}^h$ such that, for all $n = 1,\ldots,N_I$, $X^{h,n} = (\mathbf{v}^{h,n}, \mathbf{u}^{h,n})$ and $Z^{h,n} = (p^{h,n}; \varphi^{h,n}, \lambda^{h,n})$ satisfy Eq. (41) on $[t^{n-1},t^n] = I_n \subset I$, for any $(\mathbf{y}_1^h, \mathbf{y}_2^h) = Y^h \in \mathscr{Y}_{\mathbf{0}}^h$ and $(q_1^h, q_2^h, \mathbf{q}^h) = Q^h \in \mathscr{Z}^h$.

$$\mathscr{A}_{I_n}(X^{h,n}, Y^h) + \mathscr{B}_{I_n}(Z^{h,n}, Y^h) = F_{I_n}(Y^h), \tag{41a}$$

$$\mathscr{B}_{I_n}(Q^h, LX^{h,n}) = 0, \tag{41b}$$

where the operators – $\mathscr{A}_{I_n}$, $\mathscr{B}_{I_n}$ and F_{I_n} – are defined in Eqs. (30)–(32), and the discrete spaces – $\mathscr{Y}_{I,D}^h$, $\mathscr{Y}_{\mathbf{0}}^h$, and $\mathscr{Z}^h$ – follow as the discrete variants of those defined in Section 3.4.

4.3. Solving the global system

Let f be a functional, where f is the subtraction of the equations in the coupled system (41), *i.e.*

---

[5] For consistency, if the fluid $\kappa_1(\mathcal{P}_\Lambda) < \kappa(\mathbf{v})$, we must reduce the degree of the velocity space near Dirichlet boundaries where no flux of fluid is required.

$$f(\mathbf{X}^n;\mathbf{Y}) := \mathscr{A}_{I_n}(X^{h,n},Y^h) + \mathscr{B}_{I_n}(Z^{h,n},Y^h) - F_{I_n}(Y^h) - \mathscr{B}_{I_n}(Q^h, LX^{h,n}), \tag{42}$$

where $\mathbf{X}^n = (X^{h,n}, Z^{h,n})$ are the state variables and $\mathbf{Y} = (Y, Q)$ the test functions. Consequently, the coupled system must satisfy, for any choice $\mathbf{Y} \in \mathscr{Y}^h_{\mathbf{0}} \times \mathscr{Z}^h$,

$$f(\mathbf{X}^n;\mathbf{Y}) = 0.$$

Due to the finite dimension of the test space, $\mathscr{Y}^h_{\mathbf{0}} \times \mathscr{Z}^h$, and linear dependence of f on $\mathbf{Y}$, the constraint can be satisfied by ensuring $f = 0$ for each basis function in the velocity, displacement, pressure and Lagrange multiplier spaces. The result is a vector of constraints (one for each basis function), which may be assembled into a vector function, $\mathcal{F}$, that satisfies,

$$\mathcal{F}(\mathbf{X}^n) = \mathbf{0}. \tag{43}$$

Eq. (43) may be solved using an iterative approach, such as the global Newton–Raphson method [22,19]. For convenience, let $\mathbf{X}^n$ be defined by the weighted sum of all basis functions for all state variables, *i.e.*

$$(\mathbf{X}^n)^T = \chi^n \cdot \mathbf{\Psi}_{\mathbf{X}} = \begin{pmatrix} \mathbf{v}^{h,n} \\ \mathbf{u}^{h,n} \\ p^{h,n} \\ \varphi^{h,n} \\ \lambda^{h,n} \end{pmatrix}, \quad \chi^n = \begin{pmatrix} V^n \\ U^n \\ P^n \\ \varphi^n \\ \lambda^n \end{pmatrix}, \quad \mathbf{\Psi}_{\mathbf{X}} = \begin{pmatrix} \mathbf{\Psi}_v \\ \mathbf{\Psi}_u \\ \mathbf{\Psi}_p \\ \mathbf{\Psi}_\varphi \\ \mathbf{\Psi}_\lambda \end{pmatrix}, \tag{44}$$

As a result, the iterative update to the solution $\mathbf{X}^n$ is accomplished by updating the coefficient vector, χ^n. Given an initial guess, $\chi^{n,0}$, the approximate solution $\mathbf{X}^n$ at the nth time step is,

$$(\mathbf{X}^n)^T = \lim_{k\to\infty, k\in\mathbb{N}^+} \chi^{n,k} \cdot \mathbf{\Psi}_{\mathbf{X}}, \quad \chi^{n,k} := \chi^{n,k-1} + \alpha^k \delta\chi^{n,k},$$

where the scalar vector $\delta\chi^{n,k}$ is the Newton update and α^k a scalar parameter. The Newton update, $\delta\chi^{n,k}$, is selected as the solution to Eq. (45), where $\nabla_{\chi^{n,k-1}}$ is the gradient with respect to each scalar coefficient of $\chi^{n,k-1}$, $\nabla_{\chi^{n,k-1}}\mathcal{F}(\mathbf{X}^{n,k-1})$ the Jacobian, and $\mathbf{X}^{n,k-1} = (\chi^{n,k-1} \cdot \mathbf{\Psi}_{\mathbf{X}})^T$.

$$\nabla_{\chi^{n,k-1}}\mathcal{F}(\mathbf{X}^{n,k-1}) \cdot \delta\chi^{n,k} = -\mathcal{F}(\mathbf{X}^{n,k-1}). \tag{45}$$

Having solved Eq. (45) for $\delta\chi^{n,k}$, the scalar parameter, α^k, is selected to ensure a monotonic decrease in the residual, *i.e.*

$$\max_{\alpha^k\in(0,1]} |\mathcal{F}(\mathbf{y}^{n,k})| < |\mathcal{F}(\mathbf{y}^{n,k-1})|, \tag{46}$$

measured in the l_2-vector norm, $|\cdot|$.

4.3.1. Matrix system

Each iteration of the Newton–Raphson procedure requires that the linear system seen in Eq. (45) be solved for the update vector. This is solved by approximating the Jacobian by the block matrix $\mathscr{A}^{n,k}$,

$$\nabla_{\chi^{n,k-1}}\mathcal{F}(\mathbf{X}^{n,k-1}) \approx \mathscr{A}^{n,k} := \begin{pmatrix} \mathbf{A}^{n,k} & (\widetilde{\mathbf{B}}^{n,k})^{\mathrm{T}} \\ \mathbf{B}^{n,k} & \mathbf{0} \end{pmatrix}, \tag{47}$$

resulting in the update vector,

$$\delta\chi^{n,k} = -(\mathscr{A}^{n,k})^{-1}\mathcal{F}(\mathbf{X}^{n,k-1}). \tag{48}$$

The block matrix is composed of components $\mathbf{A}^{n,k}$, $\mathbf{B}^{n,k}$, and $\widetilde{\mathbf{B}}^{n,k}$ as shown in Eq. (47). These block components represent the contributions of the operators $\mathscr{A}_I$ and $\mathscr{B}_I$ introduced in Problem 4. As the operators, $\mathscr{A}_I$ and $\mathscr{B}_I$, are composed of fluid and solid terms, so to are the block components, *i.e.*

$$\mathbf{A}^{n,k} = \begin{pmatrix} A_v^{n,k} & 0 \\ 0 & A_u^{n,k} \end{pmatrix}, \quad \mathbf{B}^{n,k} = \begin{pmatrix} B_v^{n,k} & 0 \\ 0 & B_u^{n,k} \\ C_v & C_u \end{pmatrix}, \quad (\widetilde{\mathbf{B}}^{n,k})^T = \begin{pmatrix} (B_v^{n,k})^T & 0 & (C_v)^T \\ 0 & (\widetilde{B}_u^{n,k})^T & (C_u)^T \end{pmatrix}.$$

The fluid matrix $A_v^{n,k}$ can be written in $d \times d$ distinct blocks such that,

$$A_v^{n,k} = \begin{pmatrix} A_{v,11}^{n,k} & \cdots & A_{v,1d}^{n,k} \\ \vdots & \ddots & \vdots \\ A_{v,d1}^{n,k} & \cdots & A_{v,dd}^{n,k} \end{pmatrix}, \tag{49}$$

and $A^{n,k}_{v,lm}$ is an $N_v \times N_v$ matrix defined as (where integrals on $\Omega(t_n)$ are approximated using the domain update determined by the previous Newton iterate),

$$\left(A^{n,k}_{v,lm}\right)_{ij} = \rho m_{t^n}(\psi^j_v \mathbf{e}_m, \psi^i_v \mathbf{e}_l) + \rho \int_{t^{n-1}}^{t^n} c_\tau(\mathbf{v}^{h,n,k-1} - \mathbf{w}^{h,n,k-1}; \psi^j_v \mathbf{e}_m, \psi^i_v \mathbf{e}_l)\mathrm{d}\tau + \rho \int_{t^{n-1}}^{t^n} c_\tau(\psi^j_v \mathbf{e}_m - \mathbf{0}; \mathbf{v}^{h,n,k-1}, \psi^i_v \mathbf{e}_l)\mathrm{d}\tau$$
$$+ \mu \int_{t^{n-1}}^{t^n} a_\tau(\psi^j_v \mathbf{e}_m, \psi^i_v \mathbf{e}_l)\mathrm{d}\tau. \tag{50}$$

Further, the fluid and solid pressure blocks, $B^{n,k}_v$ and $\widetilde{B}^{n,k}_u$, are $1 \times d$ block matrices where each component, $B^{n,k}_{v,l}$, is given by,

$$\left(B^{n,k}_{v,l}\right)_{ij} = \int_{t^{n-1}}^{t^n} b_\tau(\psi^i_P, \psi^j_v \mathbf{e}_l)\mathrm{d}\tau, \tag{51}$$

and similarly for the solid component $\widetilde{B}^{n,k}_{u,l}$.

The solid system produces sub-components, $A^{n,k}_{u,lm}$, for which analytic computation of the true Jacobian contributions is complicated by the inherent non-linearity of many hyperelastic laws. Further, due to the generality required of the hyperelastic law to aptly model varying materials, a more generally applicable method is preferred.

Consequently, the d^2 solid sub-components to $A^{n,k}_u$ are computed using a finite difference approximation. Each $N_u \times N_u$ subcomponent, $A^{n,k}_{u,lm}$, may be expressed as,

$$\left(A^{n,k}_{u,lm}\right)_{ij} = \frac{1}{2\epsilon} \int_{I_n} s_\tau(\mathbf{u}^{h,+}, \psi^i_u \mathbf{e}_l) - s_\tau(\mathbf{u}^{h,-}, \psi^i_u \mathbf{e}_l)\mathrm{d}\tau + \frac{1}{2\epsilon} \int_{I_n} b^+_\tau(\varphi^{h,n,k-1}, \psi^i_u \mathbf{e}_l) - b^-_\tau(\varphi^{h,n,k-1}, \psi^i_u \mathbf{e}_l)\mathrm{d}\tau, \tag{52}$$

where $0 < \epsilon \ll 1$ is a differencing parameter (typically $\epsilon = 10^{-4}h$), $\boldsymbol{b}^+$ and $\boldsymbol{b}^-$ denote perturbations of the current domain (see Remark 4), and for any $\tau \in [t^{n-1}, t^n]$),

$$\mathbf{u}^{h,\pm}(\tau) := \mathbf{u}^{h,n,k-1}(\tau) \pm \epsilon \frac{\tau - t^{n-1}}{\Delta^n_\tau} \psi^j_u \mathbf{e}_m. \tag{53}$$

Remark 4. As the solid follows the Lagrangian formulation, integrals and gradients on Ω are functions of $\mathbf{u}_h$. Hence, to estimate the Jacobian, perturbations of $\mathbf{u}_h$ must be accounted for. Denoting the perturbed gradient and mapping Jacobian as,

$$\mathcal{G}^\pm_\tau := \left[\nabla_\eta \mathbf{u}^{h,\pm} + \mathbf{I}\right]^{-T} \nabla_\eta, \quad \mathcal{J}^\pm_\tau := \det\left|\nabla_\eta \mathbf{u}^{h,\pm} + \mathbf{I}\right|,$$

the computation of $s_\tau(\mathbf{u}^{h,+}, \psi^i_u \mathbf{e}_l)$, for example, utilizes $\mathcal{G}^+_\tau$ and $\mathcal{J}^+_\tau$ in place of $\mathcal{G}_\tau$ and $\mathcal{J}_\tau$ (and similarly for b^+).

Considering the block contributions to the Jacobian based on the solid pressure variables,

$$\left(B^{n,k}_{u,l}\right)_{ij} = \frac{1}{2\epsilon}\left[m^+_{t^n}(\psi^i_\varphi, 1) - m^-_{t^n}(\psi^i_\varphi, 1)\right], \quad \left(\widetilde{B}^{n,k}_{u,l}\right)_{ij} = \int_{I_n} b_\tau(\psi^i_\varphi, \psi^j_u \mathbf{e}_l)\mathrm{d}\tau, \tag{54}$$

where, following Remark 4,

$$m^\pm_{t^n}(\psi^i_\varphi, 1) = \int_{\Lambda_2} \psi^i_\varphi \mathcal{J}^\pm_{t^n} \, \mathbf{d}\boldsymbol{\eta}.$$

Lastly, the Lagrange multiplier is introduced by matrices C_v and C_u. These matrices are composed of $d \times d$ block matrices $C_{v,lm}$ and $C_{u,lm}$, where,

$$\left(C^n_{v,lm}\right)_{ij} = \int_{t^{n-1}}^{t^n} l_\tau(\psi^i_\lambda \mathbf{e}_l, \hat{\psi}^j_v \mathbf{e}_m)\mathrm{d}\tau, \quad \left(C_{u,lm}\right)_{ij} = \int_{t^{n-1}}^{t^n} l_\tau(\psi^i_\lambda \mathbf{e}_l, \hat{\psi}^j_u \mathbf{e}_m)\mathrm{d}\tau. \tag{55}$$

Notice that this definition of $\mathscr{A}^{n,k}$, and its sub-components, is merely an approximation of the Jacobian. To accommodate a general solid stress, a differencing scheme is adopted to give an accurate estimate of the solid contribution. Further, a first order approach is taken to incorporate the influence of fluid domain movement, as all integral terms for the fluid contribution are dependent on the ALE mapping at the $k-1$ Newton iterate, ignoring any dependence on $\mathbf{v}^{h,n,k}$. This is compensated for in the global Newton Scheme by updating the ALE motion in the selection of α^k (as we now have $\mathbf{v}^{h,n,k}$ to evaluate Eq. (46) at the kth iterate) and does not seem to affect convergence.

5. Stability estimates

Assuming solutions to the coupled system exist and are unique, *a priori* energy estimates demonstrate energy conservation of the scheme and ensure well-posedness by bounding the solutions entirely by given data. Moreover, as energy can only be *transferred* at the coupled interface (not created), the added Lagrange multiplier must not contribute to the energy bound. Either creation or destruction of energy by the Lagrange multiplier yields a scheme incapable of energy conservation.

With the method outlined, the discrete weak form coupled problem can be shown to satisfy Lemma 1, ensuring stability and mechanical energy conservation of the weak system (note, $\|\cdot\|_{n,\Omega}$ and $\|\cdot\|_{n,\Omega}$ are the norms and semi-norms on the nth Hilbert space [60], and otherwise $\|\cdot\|$ is a norm on the space given in the subscript).

Lemma 1. *Consider the discrete coupled system (41), with homogeneous Dirichlet boundary conditions. Suppose the operator s satisfies the Gårding-type inequality (Remark 5 of Appendix A), then the discrete solutions $\mathbf{v}_h^n$ and $\mathbf{u}_h^n$ satisfy,*

$$\frac{\alpha_1}{4}\|\mathbf{u}_h^n\|_{1,\Lambda_2}^2 + \varrho\|\mathbf{v}_h^n\|_{0,\Omega_1(t_n)}^2 + \alpha_a\int_0^{t_n}\|\mathbf{v}_h\|_{1,\Omega_1(\tau)}^2\,\mathrm{d}\tau \leqslant C_1\Big(\|\mathbf{u}_h^0\|_{1,\Lambda_2}^2 + \|\mathbf{v}_h^0\|_{0,\Omega_1(0)}^2 + \|\boldsymbol{f}_1\|_{L^2(I;\mathbf{H}^{-1}(\Omega_1))}^2 + \|\boldsymbol{f}_2\|_{L^\infty(I;\mathbf{H}^{-1}(\Lambda_2))}^2$$
$$+\|\boldsymbol{f}_2\|_{H^1(I;\mathbf{H}^{-1}(\Lambda_2))}^2 + C_s\Big),$$

*for any $n \in [1,N]$, where $C_1 \in \mathbb{R}^+$ is a constant independent of **u** and **v**. Stability is not guaranteed (as Ω_1 depends on the solution). However, if f_1 is spatially constant on Λ_1, and the data $f_1 \in L^2(I;\ \mathbf{L}^2(\Lambda_1))$ and $f_2 \in L^\infty(I;\ \mathbf{H}^{-1}(\Lambda_2)) \cap H^1(I;\mathbf{H}^{-1}(\Lambda_2))$, the energy estimate yields unconditional stability.*

Proof. See Appendix A. □

6. Results and discussion

Presented in this section are four tests aimed at demonstrating stability, robustness, and convergence of the coupling scheme for a variety of mesh types (tetrahedral/hexahedral, linear/curvilinear) and function spaces (general Taylor–Hood elements [28,15]). Using a simple *artificially* coupled fluid–fluid system, the importance of the third Lagrange multiplier space is highlighted. Further, the influence of non-linearities on the problem, and its impact on error is addressed. Subsequently, a convergence analysis was conducted in two fluid–solid mechanical systems. Based on this analysis, the potential benefit of using non-conforming grids on error reduction is elucidated. As many practical applications have a much stronger need for non-conformity, the method is assessed in a simplified elliptical model of the left-heart.

The numerical scheme outlined in Section 4 was coded in a parallel MPI-based Fortran90 code. The linear systems were solved using MUMPS [6], a Multifrontal Massively Parallel Solver [1]. Extensive verification – progressively testing the fluid (linear, non-linear, transient, and ALE) and solid mechanical frameworks – and convergence analyses on both fluid and solid mechanical systems can be found in [54].

6.1. Numerical behavior of the third saddle point

For linear systems (or each linearized Newton Step), the solvability of Eq. (48) depends on the invertibility of the block $\{\mathbf{A}\}$ and $\mathbf{X} = \mathbf{B}\mathbf{A}^{-1}\widetilde{\mathbf{B}}^T$ – the so-called Schur complement [41,70,23]. In the coupled mechanical system, the introduction of the Lagrange multiplier, λ, alters the structure of the Schur complement, which must maintain full rank for the solutions to the system to be unique – a direct result of the inf–sup condition (see Sections 3.3 and 4.1.3). Moreover, beyond uniqueness, understanding the coupling effect that the Lagrange multiplier introduces on problems with non-conforming grids, different interpolations, *etc.* is crucial. Analyzing the influence of these factors beyond simple linear theory within non-linear systems is vital for practical implementation and use of the method.

To assess the effects of the added Lagrange multiplier, a fluid problem was solved and subsequently partitioned in two coupled domains as seen in Fig. 3. For this problem, the system produces an internal vortex, whose symmetry is lost with increased Reynolds number ($\mathcal{R}$). Using identical grids with equal interpolations on either side (in this case $\mathbb{P}^2 - \mathbb{P}^1$), a number of Lagrange multiplier spaces may be tested, including $\mathbb{P}^0$, $\mathbb{P}^1$, discontinuous $\mathbb{P}^1$, $\mathbb{P}^2$, $\mathbb{P}^2_T$ (which, relating to the trace on the boundary, omits those nodal functions along Dirichlet boundaries), and $\mathbb{P}^3$.

As expected, $\mathbb{P}^0$, $\mathbb{P}^1$ and $\mathbb{P}^2_T$ all yielded solutions, while discontinuous $\mathbb{P}^1$, $\mathbb{P}^2$ and $\mathbb{P}^3$ over constrained the system, leading to spurious oscillations in the Lagrange multiplier. However, contrary to intuition, $\mathbb{P}^0$, $\mathbb{P}^1$ and $\mathbb{P}^2_T$ – despite widely varying richness – produce nearly equivalent degrees of coupling. This effect may be attributed to the apparent symmetry of the spaces, each of which have identical spurious modes.

For a more thorough examination, consider the same problem with the fluid on the left far richer (containing 512 hexahedral elements and $\mathbb{P}^3 - \mathbb{P}^2$ interpolation of velocity/pressure) than that on the right (containing 64 hexahedral elements and $\mathbb{P}^2 - \mathbb{P}^1$ interpolation of velocity/pressure). In this case, many more embeddings of spaces are possible, including the Lagrange multiplier spaces $\mathbb{P}^k$ embedded on the right grid, and $\mathbb{P}^k$ embedded on the left grid (where $0 \leqslant k \leqslant 4$ were attempted). The results of this analysis are quantified in Table 1 and displayed in Fig. 1.

As anticipated, embeddings of the Lagrange multiplier in identifiable subspaces of the coarser right grid (selections of $k = 0,1,2$) all produced solvable systems. Further, elimination of Dirichlet nodes using $\mathbb{P}^2_T$ versus $\mathbb{P}^2$ did not influence solvability due to the richness of the left space. While difficult to prove conclusively, choices of $k = 3,4$ also produced solutions,

---

[6] Available through http://graal.ens-lyon.fr/MUMPS/avail.html

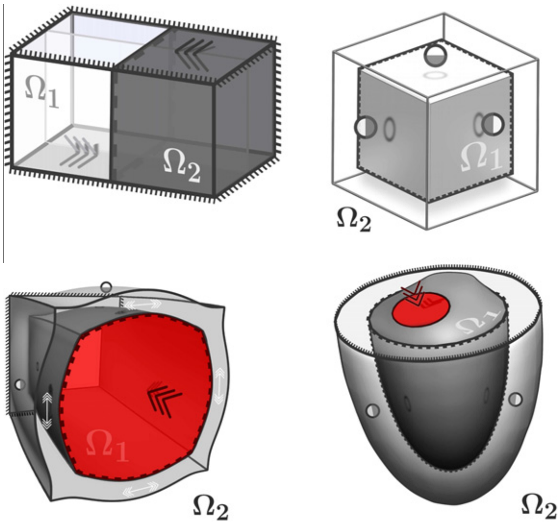

Fig. 3. Domain diagrams and boundary conditions (BC). Here the triple arrows denote flow/inflow directions, circles denote zero traction, hashes denote no slip Dirichlet conditions, and jagged lines denote coupling along marked boundaries. *(Top Left) Stress driven cavity model.* Tangential tractions are applied to the top/bottom. All side walls are no slip Dirichlet boundaries. The domain is artificially broken in half along the marked coupling boundary. *(Top Right) Fluid filled hyperelastic box model.* A displacement is prescribed (Eq. (56)) along to bottom of the box. The fluid (Ω_1) – entirely contained in the solid (Ω_2) – begins with an initial downward velocity. The zero traction is applied on all outer walls of the box. *(Bottom Left) Hyperelastic channel model.* The solid (Ω_2) has coupled/zero traction BCs on the inner/outer channel walls. The back plane of the solid is held fixed, while the front is allowed to move in plane (zero penetration and tangential traction). The fluid (Ω_1) is driven into the system by an axial traction. *(Bottom Right) Elliptical Left-Heart Model.* Held fixed on the upper planar surface, the solid (Ω_2) has coupled/zero traction BCs on the inner/outer walls. The fluid (Ω_1) is driven into the elliptical model by a prescribed Dirichlet function (red boundary). The remaining head of Ω_1 is held fixed by no slip Dirichlet conditions. (For interpretation of the references in colour in this figure legend, the reader is referred to the web version of this article.)

Table 1
$\mathbf{L}^2$– norm error on the coupling interface for varied Reynold's Number, $\mathcal{R}$ (taken as the ratio of density to viscosity), and orders of interpolation for the Lagrange Multiplier space embedded in the right domain (denoted R) and left domain (denoted L).

$\mathscr{M}^h$	$R(\mathcal{R} = 1)$	$R(\mathcal{R} = 10^2)$	$L(\mathcal{R} = 10^2)$
Error with $\mathscr{M}^h$ *of* $\|\mathbf{v}_L - \mathbf{v}_R\|_{0,\Omega}$			
1	1.62×10^{-4}	1.27×10^{-1}	9.52×10^{-3}
2	2.03×10^{-4}	1.41×10^{-1}	4.09×10^{-3}
3	1.30×10^{-3}	2.12×10^{-1}	9.99×10^{-16}[a]
4	1.28×10^{-3}	2.16×10^{-1}	Singular

[a] $\mathbb{P}^3_T$ results reported.

which is, again, most likely due to the richness of the right space. However, from Table 1, it is seen that neither of these spaces perform particularly well at coupling the two problem domains. Further, the increase in polynomial order beyond that of either trace space provides no benefit.

In contrast, choosing the Lagrange multiplier as an embedding in the richer left grid, selections of $k = 0, 1, 2$ all produce solvable systems. In this case, the elimination of Dirichlet nodes using $\mathbb{P}^3_T$ versus $\mathbb{P}^3$ is critical, as the later yields an insolvable system (as does $\mathbb{P}^4$). Moreover, embedding in the richer left grid, in all cases, produces vastly superior coupling results (see Table 1 and Fig. 4). From the linear study [57], it was suggested that the optimal space is in fact embedding the Lagrange multiplier space in the left grid using $\mathbb{P}^3_T$ functions (removing all Dirichlet nodes). Indeed, from Table 1 and Fig. 4, this choice results in vastly superior coupling results as $\mathbb{P}^3_T$ includes the trace of all functions along the boundary in each domain.

The performance of $\mathbb{P}^3_T$ is further distinguished by increased $\mathcal{R}$, seen in Table 2 and Fig. 5, where error remains below machine precision under a 100-fold increase in the Reynolds number. Perhaps even more significantly, the non-linear convergence of the method is lost when the Lagrange multiplier space is too weak relative to the kinematic trace spaces.

Many other methods for non-conforming domains, such as those proposed in [9,8], rely on prescribing functions at nodes to induce coupling. Analysis of these types of approaches have suggested that such nodal-based coupling is not optimal [11]. If the kinematic spaces differ significantly either due to mesh size or polynomial order, suboptimal coupling (particularly for non-linear systems) can negatively impact both stability and accuracy – effectively limiting the degree of non-conformity. In contrast, the method presented here is seen to be stable even when the fluid-to-solid element ratio (the average number of fluid elements paired to a solid element) is high (as seen in the final example).

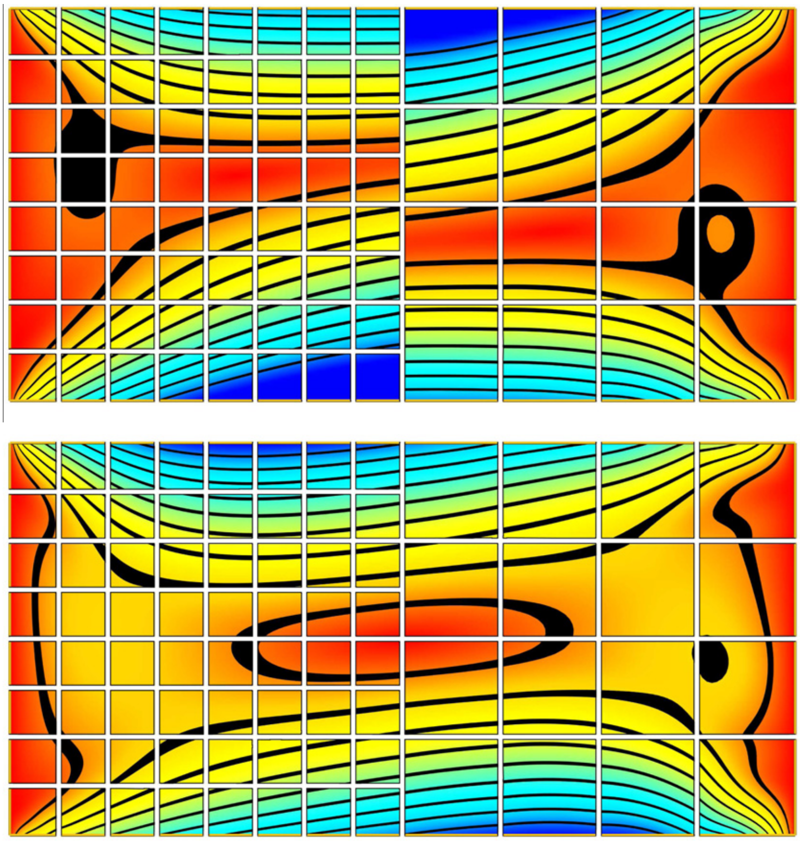

Fig. 4. Midplane view of coupled solutions using coupling Lagrange multiplier spaces using (top) $\mathbb{P}^1$ embedded in right domain, (bottom) $\mathbb{P}^3_T$ embedded in the left domain. White lines denote element boundaries. Displayed are magnitudes of velocity ranging from zero (red) to 3/10 (blue). Nine contour bands are evenly distributed through this range, labelling all velocity magnitudes in $\left[\frac{3}{10}(n/N-0.02),\ \frac{3}{10}(n/N+0.02)\right]$ black (for $n = 1,\ldots,9$ and $N = 10$). (For interpretation of the references in colour in this figure legend, the reader is referred to the web version of this article.)

Table 2
$\mathbf{L}^2$– norm error on the coupling interface for varied Reynold's Number, $\mathcal{R}$ (taken as the ratio of density to viscosity), and orders of interpolation for the Lagrange Multiplier space embedded in the left domain.

$\mathcal{R}/\mathscr{M}^h$	$\mathbb{P}^1$	$\mathbb{P}^2$	$\mathbb{P}^3_T$
Error with $\mathcal{R}$ *of* $\Vert\mathbf{v}_L-\mathbf{v}_R\Vert_{0,\Omega}$			
1	9.39E–05	4.12E–05	3.90E–18
10	9.39E–04	4.12E–04	4.86E–17
50	4.71E–03	2.06E–03	9.99E–16
100	9.52E–03	4.09E–03	9.99E–16

6.2. Convergence of the fluid–solid mechanical system

In our previous paper underpinning this work [57], optimal error estimates were shown – both theoretically and numerically – for the coupled mechanical system in the linear setting. To verify convergence properties of the coupled system in a non-linear context, two problems are considered (see Fig. 3). In the first problem, a hyperelastic box with initial momentum, is quickly decelerated leading to complex internal flows and oscillatory behavior (see Figs. 6 and 8). The second problem considers flow through a hyperelastic channel. Though this problem also exhibits oscillatory behavior, results are examined once the model reaches steady-state (gauged as maximal movement of the coupling interface of 10^{-8}). In both cases, the passive solid body is modelled as a hyperelastic Neo-Hookean material (with $C_v = 5$), and the fluid as a Newtonian (with $\rho = 1$, $\mu = 0.005$ for the hyperelastic box and $\mu = 0.0075$ for the hyperelastic channel).

The first model is that of *impact* in a fluid filled hyperelastic box, see (see Fig. 3). Starting with an initial downward velocity of $\mathbf{v} = (0, 0, -1)^T$, the momentum of the system is then curtailed by the exponential deceleration of the bottom surface of the solid (seen in Eq. (56)). As the fluid is entirely contained within the solid, this deceleration causes complex internal flows.

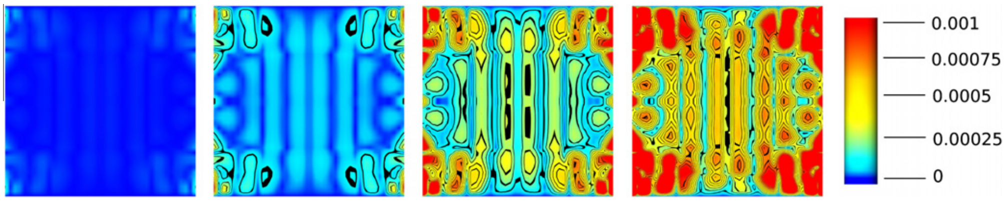

Fig. 5. Growth of error with increasing Reynolds Number, $\mathcal{R}$. Colors indicate the error between fluid velocity computed in each domain for (from left to right) $\mathcal{R} = \{1, 10, 50, 100\}$ choosing the Lagrange multiplier space to be embedded in the left domain and interpolated using $\mathbb{P}^1$ functions.

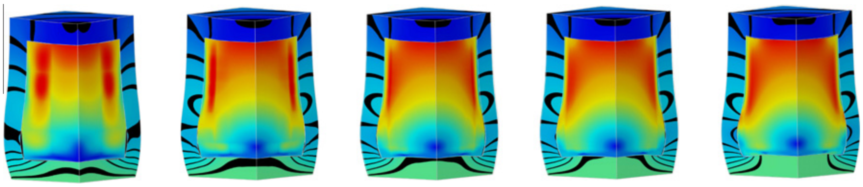

Fig. 6. Convergence of solutions to the fluid filled hyperelastic box model on various computational domains, ranging from coarsest (left) to finest (right). Magnitude of the solid is colour blue to seafoam green with contour bars to illustrate changes in the solution. Velocity magnitude of the fluid is also shown, ranging from blue to red. (For interpretation of the references in colour in this figure legend, the reader is referred to the web version of this article.)

$$\mathbf{u} = (0, 0, -u)^T, \quad u(\mathbf{x}, t) = \int_0^t |\mathbf{v}_0| e^{-\beta\tau}\, \mathrm{d}\tau, \quad \mathbf{x} \in \Upsilon_2^D. \tag{56}$$

The rate at which the solid face slows is given by the parameter β. As $\beta \to 0$, the velocity of the solid face approaches $(0,0,-1)^T$ for all time, while as $\beta \to \infty$, the velocity of the solid decays instantly (simulating true impact). As simulating true impact causes a near singularity in the temporal boundary conditions – in turn, complicating convergence analysis – a milder selection of β was used (see Fig. 8).

As the solid face slows, momentum in the fluid is, in part, dissipated by viscous effects. The remaining momentum is transformed into potential energy stored within the solid. Potential energy is seen by the displacement of the body, which distends symmetrically on all sides and pulls the upper surface downward. As momentum decays, the potential energy of the solid is returned to the fluid, causing inward flow along the sides and upward flow at the top. Once again, the momentum of the fluid causes the solid to distend (this time inward on the sides and outward on the top), and the system continues to oscillate until all energy has been dissipated by viscous effects (see Fig. 8). In the limit, as $t \to \infty$, the solution to the system is a stagnant fluid with the hyperelastic box with $\mathbf{u} = (0,0,--\mathbf{v}_0-/\beta)^T$.

To assess convergence of the coupled model, five (fluid/solid) tessellations with (64/96), (216/216), (512/768), (4095/6144), and (20,736/13,824) hexahedral elements were used. The velocity/pressure in the fluid and displacement/pressure in the solid were both interpolated using $\mathbb{P}^2 - \mathbb{P}^1$ Taylor–Hood functions. The spatial map of the fluid–solid system was taken as trilinear and triquadratic, respectively. The third Lagrange multiplier space was selected as an embedding of the fluid trace space using $\mathbb{P}^2$ functions (note that, as no Dirichlet conditions are present $\mathbb{P}^2$ yields the same space as $\mathbb{P}^2_T$). Solutions for the first four discretizations were compared at $t = 0.1$ with the finest grid solution (ran with $\Delta_\tau 1 \times 10^{-4}$). Solutions on the various grids are seen in Fig. 6, while the measures of error are supplied in Table 3.

Table 3
Maximum $\mathbf{L}^2-$ norm and $\mathbf{H}^1-$ semi-norm between fluid and solid domains at time $t = 0.1$. Columns indicate the norm values on various grid refinements, while rows scale temporally as powers of h. The final column gives the optimal scaling based on interpolation theory.

Δ_t/h	1/2 $\|\cdot\|_0$	1/3 $\|\cdot\|_0$	1/4 $\|\cdot\|_0$	1/8 $\|\cdot\|_0$	$\mathcal{O}$
Convergence of max($\|\mathbf{v} - \mathbf{v}_h\|_{0,\Omega}$, $\|\mathbf{u} - \mathbf{u}_h\|_{0,\Omega}$)					
h	1.09×10^{-3}	7.87×10^{-4}	5.98×10^{-4}	3.13×10^{-4}	h
h^2	1.09×10^{-3}	5.46×10^{-4}	2.99×10^{-4}	6.45×10^{-5}	h^2
h^3	1.09×10^{-3}	3.81×10^{-4}	1.41×10^{-4}	1.00×10^{-5}	h^3
Δ_t/h	1/2 $|\cdot|_1$	1/3 $|\cdot|_1$	1/4 $|\cdot|_1$	1/8 $|\cdot|_1$	$\mathcal{O}$
Convergence of max($|\mathbf{v} - \mathbf{v}_h|_{1,\Omega}$, $|\mathbf{u} - \mathbf{u}_h|_{1,\Omega}$)					
h	1.34×10^{-2}	8.32×10^{-3}	6.31×10^{-3}	3.42×10^{-3}	h
h^2	1.34×10^{-2}	6.79×10^{-3}	4.19×10^{-3}	1.75×10^{-3}	h^2
h^3	1.34×10^{-2}	5.97×10^{-3}	3.41×10^{-3}	1.72×10^{-3}	h^2

The hyperelastic channel model (see Fig. 3) begins with a quiescent fluid and solid, which is subjected to an axial pressure gradient. With time, the channel dilates; however this process is heavily influenced by the momentum of the fluid, causing over and under dilation relative to the eventual steady-state (reached after 20 s). A unit inward traction was applied to one end of the channel, causing a peak velocity of ~2 and $\mathcal{R} \sim 130$. The approximate percentage strain in the solid mechanical model (taken as the maximal displacement over inner channel dimension) was ~50%.

To assess the convergence of the model for varying levels of non-conformity, four fluid and four solid tessellations with $\{4, 32, 256, 2048\}$ and $\{12, 40, 320, 2560\}$ hexahedral elements were coupled in different combinations to approximate the solution. Both fluid and solid bodies were interpolated using $\mathbb{P}^2 - \mathbb{P}^1$ Taylor–Hood functions. In each case, the third Lagrange multiplier space was selected as an embedding of richest trace space using $\mathbb{P}^2_T$ functions. Further, both domains used triquadratic spatial maps. Solutions on the various grids are shown in Fig. 7. The error, measured relative to the finest grid, is reported in Table 4.

Convergence of the method is demonstrated in both the hyperelastic box and channel examples (see Tables 3 and 4). In these examples, the interpolation spaces are $\mathbb{P}^2 - \mathbb{P}^1$; which, under optimal convergence conditions [6,60,57], should lead to error convergence scaling like h^2 and h^1 in the $\mathbf{L}^2$ and $\mathbf{H}^1$-norms, respectively. However, these results are limited by the Lagrange multiplier spaces. Indeed, within the displacement/velocity spaces there are projections (such as the $\mathbf{H}^1$-projection) which converge like h^3 and h^2 in the $\mathbf{L}^2$ and $\mathbf{H}^1$-norms. As the method outlined takes an implicit Euler approach to temporal discretization, error in the hyperelastic box (see Table 3) shows that, for appropriate scaling of the temporal discretization parameter, optimal error convergence rates are observed. Indeed, these results show convergence rates closer to that of the optimal projection, suggesting it is nearly weakly divergence free.

While convergence in the hyperelastic box model was assessed by further refining an initial model, in the hyperelastic channel model, convergence is considered for different mesh discretizations. Certainly, optimal convergence is again seen in Table 4 along the diagonal (corresponding to equivalent refinement of the entire model). However, Table 4 also demonstrates the utility of the non-conforming domains, as the error stems predominantly from error in the fluid model. Examining the last row of Table 4 the model coupling the coarsest solid and finest (excluding the benchmark grid) fluid produces an $\mathbf{H}^1$ error of 1.14×10^{-1}, while coupling the finest fluid and solid grids (excluding the benchmark grid) – effectively increasing the system size ~215% – gives nearly equivalent error. As a result, using varying refinement provides a much more efficient means to solve the system, while maintaining coupling accuracy to machine precision.

6.3. Elliptical left-heart model

To demonstrate the functionality of the method for more complex problems, both in terms of non-conformity of the interface as well as the non-linearity of the system, a simplified elliptical model of the left ventricle of the heart is considered (see Fig. 3). In this model, flow is driven into a hyperelastic chamber, simulating the conditions common under diastolic filling of the left ventricle. The fluid is modelled as Newtonian (with a $\mathcal{R} \sim 1,000$) on an anisotropic linear tetrahedral grid (using $\mathbb{P}^2 - \mathbb{P}^1$ interpolation of velocity and pressure) consisting of 21,000 elements. The solid, an anisotropic Neo-Hookean material is modelled on a curvilinear hexahedral grid (using $\mathbb{P}^3 - \mathbb{P}^1$ interpolation for displacement and pressure) consisting of 180 elements. The quasi-static formulation is used in this example. This may be justified by a simple dimensional analysis which shows that the rate of momentum in the fluid dominates that observed in the solid.

The third Lagrange multiplier is selected as an embedding in the richer fluid space using $\mathbb{P}^2_T$. While the coupling interface from the fluid side is composed of 1920 triangular elements, the solid side consists of only 180. Due to the anisotropic nature of the tetrahedral grid, the ratio of fluid-to-solid elements ranges from 4 to 64. Results of this simulation at various time points in the diastolic period are shown in Fig. 9.

While the previous examples demonstrate the methods functionality, the elliptical left-heart model shows that this behavior holds under even more complex conditions. Not only are the inherent interpolation spaces different but the discretization sizes widely differ. The model problem also exhibits much more complex dynamics due to the increased non-linearity of the fluid model. Under these conditions, the method is still seen to perform well, yielding precise (to machine precision) coupling.

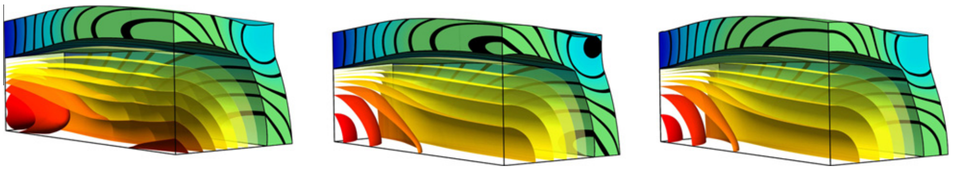

Fig. 7. Convergence of upper quadrant solutions to the steady-state hyperelastic channel model at different grid resolutions: *(Left)* coarsest fluid and solid models, *(Middle)* finest fluid and coarsest solid models, *(Right)* benchmark fine grid solution. In the fluid, isoplanes of velocity magnitude are shown ranging from 0.2 (translucent green-yellow) to 1.6 (red) in increments of 0.2. The solid displacement magnitude is plotted ranging from 0 (blue) to 0.1 (seafoam green). Nine contour lines, marked in black, are evenly distributed in the range [0, 0.14]. (For interpretation of the references in colour in this figure legend, the reader is referred to the web version of this article.)

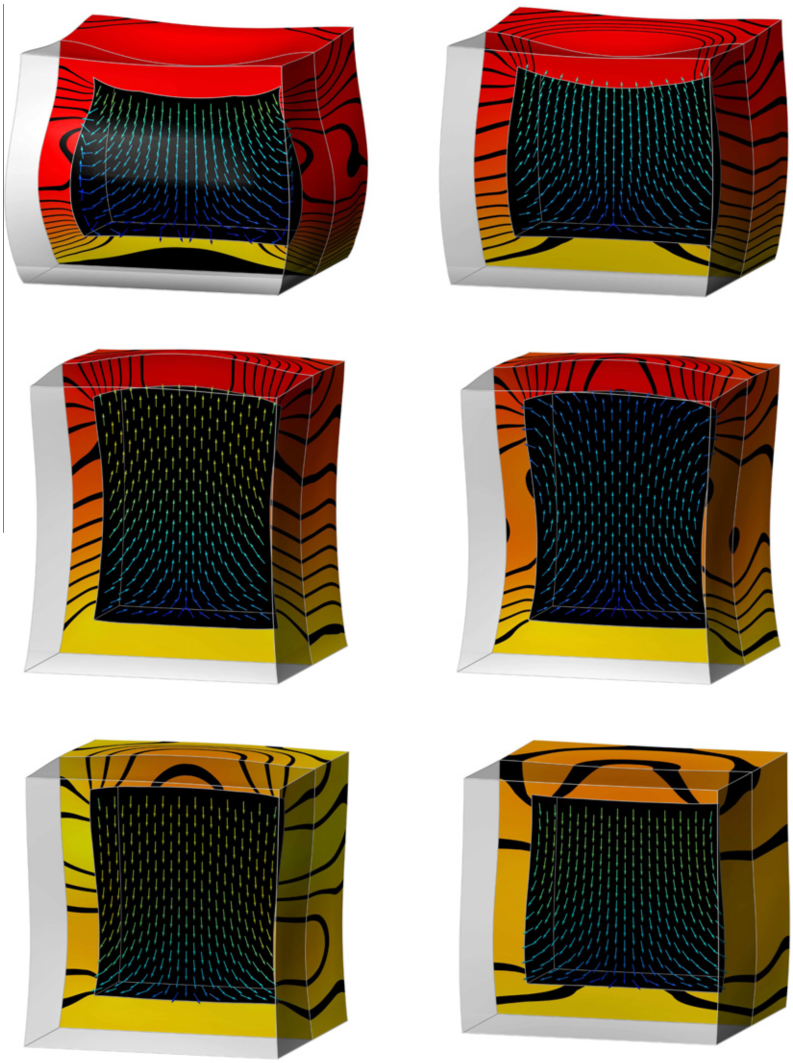

Fig. 8. Fluid and solid solutions for the 'Impact in a Fluid Filled Hyperelastic Box' problem at (left side top to bottom, right side top to bottom) times $t = \{\frac{1}{4}, \frac{3}{4}, \frac{5}{4}, \frac{7}{4}, \frac{9}{4}, \frac{11}{4}\}$. Vector arrows denoting the direction of flow are shown on the mid-line of the domain and are colored according to velocity magnitudes (ranging from (blue) zero to (seafoam green) $\sim \frac{1}{2}$). The deformed solid body is colored according to displacement magnitude (ranging from (yellow) zero to (red) $\sim \frac{1}{10}$). Nineteen contour bands are evenly distributed through this range, labelling all solid displacement magnitudes in $\left[\frac{3}{20}(n/N - 0.01),\ \frac{3}{20}(n/N + 0.01)\right]$ black (for $n = 1, \ldots, 19$ and $N = 20$). (For interpretation of the references in colour in this figure legend, the reader is referred to the web version of this article.)

7. Conclusion

In this paper, a monolithic technique was introduced for problems of coupled mechanics. This technique, through the use of a third Lagrange multiplier, allows for accurate coupling (in many cases to machine precision) of highly non-conforming domains, while preserving stability properties typically enjoyed by other monolithic schemes. The method is also shown to converge optimally based on error estimates derived for simpler linear systems. The freedom of this non-conformity allows for the coupling of function spaces and tessellations independently tailored for the physics of the model. For example, in biomechanical systems, such as the sample system of Section 6.3, where the characteristic behavior of fluids and solids demand disparate discretization schemes, non-conformity of the coupling bodies provides an accurate and efficient numerical approach for simulations. Though the Lagrange multiplier introduces additional degrees of freedom, these generally make up a small portion of the overall problem size – particularly for physically relevant problems which require high refinement.

Using a third Lagrange multiplier, in this study a technique was presented for the coupling of mechanical bodies. The introduction of an additional Lagrange multiplier requires the development of an appropriate function space. From the linear theory developed [57], an embedding of either the fluid or solid trace space satisfies the inf–sup condition. In this paper we demonstrate that for practical non-linear problems, optimal results are obtained when the Lagrange multiplier space is

Table 4
$\mathbf{H}^1$–-norm of error in the fluid–solid model at steady-state. Columns indicate the error seen with successive refinement of the solid model ($\hbar$), while rows give error with refinement of the fluid model (h). Though the domain refinement was halved for each refinement, due to the deformation in the model, this lead to mesh sizes of $h, \hbar \sim \{0.53, 0.34, 0.19\}$. The last column and row give the expected error based on optimal convergence in h and $\hbar$, respectively. As is clear, the error in the fluid model is dominant (the solid error was approximately two orders of magnitude lower than that of the fluid while the magnitude in displacement/ velocity was only an order of magnitude different), following the optimal convergence trend with strictly h refinement (compare column 1/2 with $\mathcal{O}(h^2)$).

$h/\hbar$	1/2	1/4	1/8	$\mathcal{O}(h^2)$
Convergence of $(\lVert\mathbf{v}-\mathbf{v}_h\rVert^2_{1,\Omega_1}+\lVert\mathbf{u}-\mathbf{u}_h\rVert^2_{1,\Omega_2})^{1/2}$				
1/2	6.52×10^{-1}	6.39×10^{-1}	6.32×10^{-1}	–
1/4	2.84×10^{-1}	2.77×10^{-1}	2.75×10^{-1}	2.74×10^{-1}
1/8	1.14×10^{-1}	9.68×10^{-2}	9.09×10^{-2}	9.11×10^{-2}
$\mathcal{O}(\hbar^2)$	–	2.74×10^{-1}	9.11×10^{-2}	

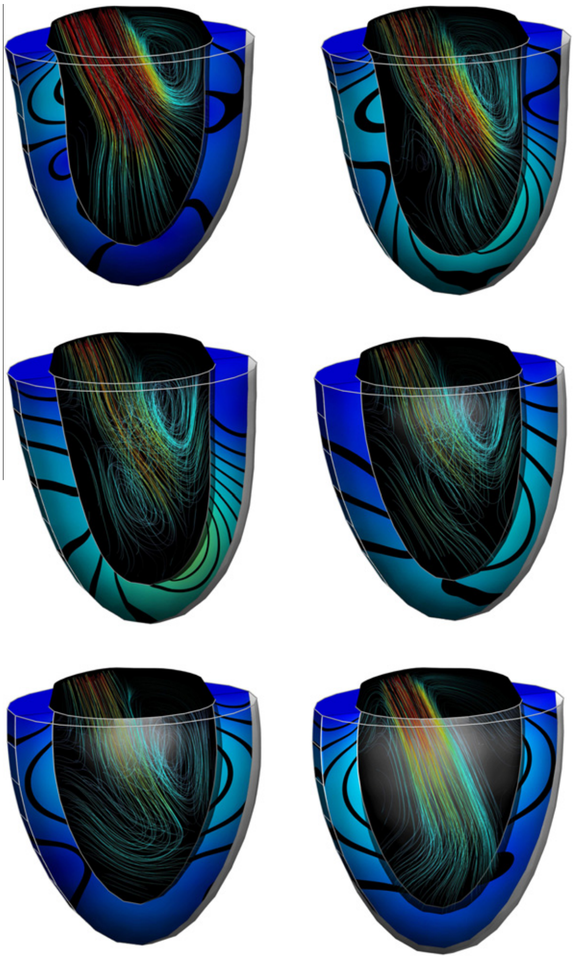

Fig. 9. Solutions to the coupled fluid–solid elliptical left-heart model at times *(Top Left)* 0.15 s, *(Top Right)* 0.2 s, *(Middle Left)* 0.25 s, *(Middle Right)* 0.3 s, *(Bottom Left)* 0.35 s, and *(Bottom Right)* 0.45 s. The overall filling cycle occurs over a time period of 0.5 s. The fluid solution is displayed as streamlines through the vector field at the specified time, with colors indicating the magnitude of flow from 0 (blue) to 0.5 m/s (red). The solid is sectioned in half, displaying displacement magnitude on all walls ranging from 0 blue to 0.01 m (seafoam green). (For interpretation of the references in colour in this figure legend, the reader is referred to the web version of this article.)

selected as the richest embedding. Further, weaker spaces are shown to negatively impact non-linear convergence as the kinematic variables are not sufficiently constrained on the boundary. These results are demonstrated in a simple elliptical heart model, showing the fidelity of the approach for a highly non-linear problem under varied fluid and solid discretizations.

Beyond enhancing the flexibility of mesh and basis function selection for each mechanical problem, the Lagrange multiplier approach makes the process of multi-domain coupling straightforward. Though the examples presented focused on the coupling of a single fluid and solid domain, the method can be easily extended to consider the coupling of multiple bodies. This is particularly useful for more complex problems which consist of multiple solids and fluids with varied mechanical properties. As the increase in problem size due to the additional Lagrange multiplier is small (amounting to 5–10% of the total system size in all refined examples presented), this approach allows for the efficient coupling of multiple physical problems at minimal cost.

Though the presented method provides a number of benefits, there are still many opportunities for further advancement and investigation of the approach. An area of particular concern is the solution of the linear system in Eq. (48), which accounts for much of the CPU time. Though this paper focuses on the theoretical results and convergence of the Lagrange multiplier coupling scheme, extensive research has been presented on the efficient solution of the linear problem for mechanical [23,41,58] and coupled mechanical systems [35,36]. Of note is the recent work of Heil [36], who – using preconditioned iterative solvers – shows that the efficient solution of monolithic systems often outperforms partitioned alternatives. With further advancements to linear solution approaches, the coupling technique presented provides an effective means for the quantitative evaluation of multi-physics problems.

Acknowledgements

The authors would like to thank the editor and reviewers for their assistance with this manuscript. The authors would like to acknowledge support from the United Kingdom Engineering and Physical Sciences Research Council (FP/F059361/1), British Heart Foundation (PG/08/122), the European Commission (FP7-ICT-2007-224495: euHeart), and the Whitaker International Fellows program. The authors also acknowledge Oxford Supercomputing Centre (OSC) for their computational support.

Appendix A. *A priori* stability proof

In this supplement, we prove Lemma 1 of Section 5. We will also show that the condition of Lemma 1, Remark 5, is satisfied for a Neo-Hookean material. We begin by noting Remark 5 and the following Lemma [54].

Remark 5. Gårding-type Inequality for the Solid OperatorLet the form s, stemming from Eq. (24), satisfy, for any $[a,b] \in I$,

$$\alpha_1 |\mathbf{u}_h(b)|^2_{1,\Lambda} - \alpha_2 |\mathbf{u}_h(a)|^2_{1,\Lambda} \leqslant \int_a^b s_\tau(\mathbf{u}, \partial_t \mathbf{u}) \mathrm{d}\tau + C_s, \tag{57}$$

where $\alpha_1,\ \alpha_2,\ C_s \in \mathbb{R}^+$ are a constants independent of $\mathbf{u}$.

Lemma 2. *Let $0 \leqslant (g,c,f) \in I = [0,T]$, be a positive functions on the time interval I, and $f \in L^2(I)$, $c \in L^\infty(I)$. Then, if for any $t \in I$, g satisfies the estimate*

$$g(t) \leqslant c(t) + \int_0^t f(\tau) g^{1/2}(\tau) \mathrm{d}\tau,$$

then $g \in L^\infty(I)$ satisfies, for any $t \in I$,

$$g(t) \leqslant 2\|c\|_{L^\infty(I)} + I\|f\|^2_{0,I}.$$

Now consider the homogeneous Dirichlet problem, where the velocity (as well as fluid domain velocity) and displacement are zero on Γ_1^D and Γ_2^D, respectively. Further, $\Gamma_1^N = \{\emptyset\}$ and $\Gamma_2^N = \{\emptyset\}$. The fluid and solid satisfy the ALE Navier–Stokes equation and quasi-static finite elasticity equations as set out in Eq. (41), allowing us to prove Lemma 1.

Proof Lemma 1. To show the stability result of Lemma 1, we choose $Y^h = LX^{h,n}$ in Eq. (41a) and $Q^h = Z^{h,n}$ in Eq. (41b), giving the equality,

$$\mathscr{A}_{I_n}(X^{h,n}, LX^{h,n}) = F_{I_n}(X^{h,n}), \tag{58}$$

over the in the time interval I_n. Using the definition of $\mathscr{A}$ and F in Eqs. (30) and (32), the inequality (59) may be derived following the estimates in Quarteroni and Nobile [60,53] (where $\alpha_a = \mu / C_{\Lambda_1}$, is the coercivity constant and C_{Λ_1} is the Poincare Constant).

$$\begin{aligned} &\frac{\rho}{2}\|\mathbf{v}^{h,n}\|^2_{0,\Omega_1(t^n)} + \int_{t^{n-1}}^{t^n} s_\tau(\mathbf{u}^h, \partial_t \mathbf{u}^h)_{\Lambda_2} \mathrm{d}\tau + \alpha_a \int_{t^{n-1}}^{t^n} \|\mathbf{v}^{h,n}\|^2_{1,\Omega_1(\tau)} \mathrm{d}\tau \\ &\quad \leqslant \frac{\rho}{2}\|\mathbf{v}^{h,n-1}\|^2_{0,\Omega_1(t^{n-1})} + \int_{t^{n-1}}^{t^n} m_\tau(f_{\ 1}, \mathbf{v}^{h,n}) + M_{\ \tau}(f_{\ 2}, \partial_t \mathbf{u}^h) \mathrm{d}\tau. \end{aligned} \tag{59}$$

As we may similarly arrive at inequality (59) for $t^{n-1}, t^{n-2}, \ldots$ by summing (and adding the viscous fluid and solid stress terms over the previous time interval to each side) we arrive at,

$$\frac{\rho}{2}\|\mathbf{v}^{h,n}\|^2_{0,\Omega_1(t^n)} + \alpha_s\|\mathbf{u}^{h,n}\|^2_{1,\Lambda_2} + \alpha_a\int_0^{t^n}\|\mathbf{v}^{h,n}\|^2_{1,\Omega_1(\tau)}\,\mathrm{d}\tau \leqslant \frac{\rho}{2}\|\mathbf{v}^{h,0}\|^2_{0,\Omega_1(0)} + \alpha_s\|\mathbf{u}^{h,0}\|^2_{1,\Lambda_2} + \int_0^{t^n}\boldsymbol{m}_\tau(\boldsymbol{f}_1,\mathbf{v}^{h,n})\mathrm{d}\tau + C_s + \int_0^{t^n}\boldsymbol{M}_\tau(\boldsymbol{f}_2,\partial_t\mathbf{u}^h)\mathrm{d}\tau. \tag{60}$$

Here we have used the fact that the solid operator, s_τ, satisfies the Gårding-type inequality shown in Eq. (57). Noting,

$$\int_0^{t^n}\boldsymbol{m}_\tau(\boldsymbol{f}_1,\mathbf{v}^{h,n})\mathrm{d}\tau \leqslant \frac{1}{2\alpha_a}\int_0^{t^n}\|\boldsymbol{f}_1\|^2_{0,\Omega_1(\tau)}\,\mathrm{d}\tau + \frac{\alpha_a}{2}\int_0^{t^n}\|\mathbf{v}^{h,n}\|^2_{1,\Omega_1(\tau)}\,\mathrm{d}\tau \tag{61}$$

and, as f_2 is sufficiently smooth, using integration by parts,

$$\int_0^{t^n}\boldsymbol{M}_\tau(\boldsymbol{f}_2,\partial_t\mathbf{u}^h)\mathrm{d}\tau = \boldsymbol{M}_{t^n}(\boldsymbol{f}_2,\mathbf{u}^h) - \boldsymbol{M}_0(\boldsymbol{f}_2,\mathbf{u}^h) - \int_0^{t^n}\boldsymbol{M}_\tau(\partial_t\boldsymbol{f}_2,\mathbf{u}^h)\mathrm{d}\tau \leqslant \frac{1}{2\alpha_s}\|\boldsymbol{f}_2(t^n)\|^2_{-1,\Lambda_2} + \frac{\alpha_s}{2}\|\mathbf{u}^{h,n}\|^2_{1,\Lambda_2} + \|\boldsymbol{f}_2(0)\|_{-1,\Lambda_2}\|\mathbf{u}^{h,0}\|_{1,\Lambda_2} + \frac{1}{2}\int_0^{t^n}\|\partial_t\boldsymbol{f}_2\|^2_{-1,\Lambda_2}\,\mathrm{d}\tau + \frac{1}{2}\int_0^{t^n}\|\mathbf{u}^h\|^2_{1,\Lambda_2}\,\mathrm{d}\tau, \tag{62}$$

Eq. (60) may be re-written as,

$$\rho\|\mathbf{v}^{h,n}\|^2_{0,\Omega_1(t^n)} + \alpha_s\left\|\mathbf{u}^{h,n}\right\|^2_{1,\Lambda_2} + \alpha_a\int_0^{t^n}\left\|\mathbf{v}^{h,n}\right\|^2_{1,\Omega_1(\tau)}\mathrm{d}\tau \leqslant C\left(\left\|\mathbf{v}^{h,0}\right\|^2_{0,\Omega_1(0)} + \left\|\mathbf{u}^{h,0}\right\|^2_{1,\Lambda_2}\right) + g(t^n) + \int_0^{t^n}\left\|\mathbf{u}^h\right\|^2_{1,\Lambda_2}\mathrm{d}\tau. \tag{63}$$

where $C > 0$ is a constant independent of time, and $g(t) \geqslant 0$ is the strictly positive functional,

$$g(t^n) = C_s + \int_0^{t^n}\|\boldsymbol{f}_1\|^2_{0,\Omega_1(\tau)}\,\mathrm{d}\tau + \frac{1}{\alpha_s}\|\boldsymbol{f}_2(t^n)\|^2_{-1,\Lambda_2} + \int_0^{t^n}\|\partial_t\boldsymbol{f}_2\|^2_{-1,\Lambda_2}\,\mathrm{d}\tau. \tag{64}$$

Note that g depends not only on the initial data, the reference domains and time, but also $\Omega_1(\tau)$, itself an implicit function of the solution, $\mathbf{v}^h$. Applying Lemma 2, we may obtain the first part of Lemma 1. To remove the dependence on Ω_1, assuming f_1 is a constant in space, noting the SCL and an applying divergence theorem, we arrive at the transformation,

$$\|\boldsymbol{f}_1(t^n)\|^2_{0,\Omega_1(t^n)} - \|\boldsymbol{f}_1(t^n)\|^2_{0,\Omega_1(0)} = \int_0^{t^n}\int_{\Lambda_1}|\boldsymbol{f}_1(t^n)|^2\mathcal{G}_\tau\cdot\mathbf{w}^h\mathcal{J}_{\Omega_1,\tau}\,\mathbf{d}\boldsymbol{\eta}\,\mathrm{d}t \tag{65}$$

for which the *RHS* is zero. As a consequence, the solution is entirely bound by given data, and is thus unconditionally stable. □

An example of a material for which the operator s_τ satisfies the restriction imposed by Property 5 is noted in the following remark.

Remark 6. An example of a solid operator, s_τ, satisfying Property 5 is that induced by a so-called Neo-Hookean material, where,

$$\sigma(\mathbf{u}(\tau)) = c_\sigma\left(\mathbf{F}_\tau\mathbf{F}_\tau^{\mathrm{T}} - \frac{1}{3}\mathbf{F}_\tau : \mathbf{F}_\tau\mathbf{I}\right), \tag{66}$$

Here, $\mathbf{F}_\tau$, a function of displacement, is given by Eq. (9) and $c_\sigma > 0$ is a constant. In the discrete setting, the modified Neo-Hookean, given by,

$$\sigma\left(\mathbf{u}^h(\tau)\right) = c_\sigma\left(\mathbf{F}_\tau\mathbf{F}_\tau^{\mathrm{T}} - \frac{1}{3}\mathcal{J}_{\Omega_2,\tau}\vartheta\mathbf{I}\right), \tag{67}$$

satisfies Property 5, where ϑ is the L^2-projection of $\mathbf{F}_\tau : \mathbf{F}_\tau/\mathcal{J}_{\Omega_2,\tau}$ into the interpolation space $\mathcal{W}(\Lambda_2)$.

Proof Remark 6. The proof of remark follows from Eqs. (9), (24), and (66). In the continuous case, the solid operator may be written as,

$$\int_{t^{n-1}}^{t^n}\boldsymbol{s}_\tau(\mathbf{u}^h,\mathbf{u}^{h,n}-\mathbf{u}^{h,n-1})\mathrm{d}\tau = \int_{t^{n-1}}^{t^n}\boldsymbol{s}_\tau(\mathbf{u}^h,\partial_t\mathbf{u}^h)\Lambda_2\,\mathrm{d}\tau = c_\sigma\int_{t^{n-1}}^{t^n}\int_{\Lambda_2}\left(\mathbf{F}_\tau\mathbf{F}_\tau^{\mathrm{T}} - \frac{1}{3}(\mathbf{F}_\tau : \mathbf{F}_\tau)\mathbf{I}\right) : \mathcal{G}_\tau\partial_t\mathbf{u}^h\,\mathbf{d}\boldsymbol{\eta}\,\mathrm{d}\tau \tag{68}$$

We note, however, that,

$$\mathcal{G}_\tau\partial_t\mathbf{u}^h = \nabla_\eta\partial_t\mathbf{u}^h\mathbf{F}_\tau^{-1} = \partial_t\mathbf{F}_\tau\mathbf{F}_\tau^{-1} \tag{69}$$

as the gradient operator in Λ_1 and the Lagrangian time derivative commute. Further, noting that by the SCL and solid incompressibility condition, the second part of the Neo-Hookean model is zero, *i.e.*

$$c_\sigma \int_{t^{n-1}}^{t^n} \int_{\Lambda_2} \left(\frac{1}{3} (\mathbf{F}_\tau : \mathbf{F}_\tau) \mathbf{I} \right) : \mathcal{G}_\tau \partial_t \mathbf{u}^h \, \mathbf{d}\boldsymbol{\eta} \, \mathrm{d}\tau = 0. \tag{70}$$

As the discrete formulation projects this term into the saddle space $\mathcal{W}(\Lambda_2)$, Eq. (70) holds in both settings. Plugging this into (68), and applying integration by parts,

$$\begin{aligned} c_\sigma \int_a^b \int_{\Lambda_2} \mathbf{F}_\tau \mathbf{F}_\tau^{\mathrm{T}} : \partial_t \mathbf{F}_\tau \mathbf{F}_\tau^{-1} \, \mathbf{d}\boldsymbol{\eta} \, \mathrm{d}\tau &= c_\sigma \int_a^b \int_{\Lambda_2} \mathbf{F}_\tau : \partial_t \mathbf{F}_\tau \, \mathbf{d}\boldsymbol{\eta} \, \mathrm{d}\tau \\ &= \frac{c_\sigma}{2} \left(\|\mathbf{F}_b\|_{0,\Lambda}^2 - \|\mathbf{F}_a\|_{0,\Lambda}^2 \right) \geqslant \frac{c_\sigma}{2} \left([1-\epsilon_1] |\mathbf{u}(b)|_{1,\Lambda}^2 - [1+\epsilon_2] |\mathbf{u}(a)|_{1,\Lambda}^2 - \left[\frac{1}{\epsilon_1} + \frac{1}{\epsilon_2} \right] \|\mathbf{I}\|_{0,\Lambda}^2 \right) \\ &\geqslant \alpha_1 |\mathbf{u}(b)|_{1,\Lambda}^2 - \alpha_2 |\mathbf{u}(a)|_{1,\Lambda}^2 - C_s \end{aligned} \tag{71}$$

where Triangle and Young's Inequalities were used to derive the identities (for a general tensor **A** and **B**),

$$(1-\epsilon_1)\|\mathbf{A}\|^2 + \left(1 - \frac{1}{\epsilon_1}\right)\|\mathbf{B}\|^2 \leqslant \|\mathbf{A}+\mathbf{B}\|^2 \leqslant (1+\epsilon_2)\|\mathbf{A}\|^2 + \left(1 + \frac{1}{\epsilon_2}\right)\|\mathbf{B}\|^2. \tag{72}$$

Selecting $\epsilon_1 = \epsilon_2 = 1/2$, the constants of Remark 5 are simply $C_s = 2c_\sigma \|\mathbf{I}\|_{0,\Lambda}^2$, $\alpha_1 = c_\sigma/4$, and $\alpha_2 = 3c_\sigma/4$. □

References

[1] P. Amestoy, I. Duff, J. L'Excellent, Multifrontal parallel distributed symmetric and unsymmetric solvers, Comput. Methods Appl. Mech. Eng. 184 (2000) 501–520.
[2] C. Antoci, M. Gallati, S. Sibilla, Numerical simulation of fluid–structure interaction by sph, Comput. Struct. 85 (2007) 879–890.
[3] T. Arbogast, L. Cowsar, M. Wheeler, I. Yotov, Mixed finite element methods on nonmatching multiblock grids, SIAM.J. Numer. Anal. 37 (2000) 1295–1315.
[4] T. Arbogast, I. Yotov, A non-mortar mixed finite element method for elliptic problems on non-matching multiblock grids, Comput. Methods Appl. Mech. Eng. 149 (1997) 255–265.
[5] F. Baaijens, A fictitious domain/mortar element method for fluid–structure interaction, Int. J. Numer. Methods Fluids 35 (2001) 743–761.
[6] I. Babuska, The finite element method with Lagrange multipliers, Numer. Math. 20 (1973) 179–192.
[7] I. Babuska, E. Podnos, G. Rodin, New fictitious domain methods: Formulation and analysis, Math. Models Methods Appl. Sci. 15 (2005) 1575–1594.
[8] K. Bathe, G. Ledezma, Benchmark problems for incompressible fluid flows with structural interactions, Comput. Struct. 85 (2007) 628–644.
[9] K. Bathe, H. Zhang, Finite element developments for general fluid flows with structural interactions, Int. J. Numer. Methods Eng. 60 (2004) 213–232.
[10] F. Belgacem, C. Bernardi, N. Chorfi, Y. Maday, Inf–sup conditions for the mortar spectral element discretization of the Stokes problem, Numer. Math. 85 (2000) 257–281.
[11] F. Belgacem, P. Hild, P. Laborde, The mortar finite element method for contact problems, Math. Comput. Model. 28 (1998) 263–271.
[12] F. Bertrand, P. Tanguy, F. Thibault, A three-dimensional fictitious domain method for incompressible fluid flow problems, Int. J. Numer. Methods Fluids 25 (1997) 719–736.
[13] J. Bonet, R. Wood, Nonlinear Continuum Mechanics for Finite Element Analysis, Cambridge University Press, 1997.
[14] F. Brezzi, On the existence, uniqueness and approximation of saddle-point problems arising from Lagrange multipliers, R.A.I.R.O. 2 (1974) 129–151.
[15] F. Brezzi, M. Fortin, Mixed and Hybrid Finite Element Methods, Springer-Verlag, Heidelberg, 1991.
[16] M. Cervera, R. Codina, M. Galindo, On the computational efficiency and implementation of block-iterative algorithms for nonlinear coupled problems, Eng. Comput. 13 (1994) 4–30.
[17] Y. Cheng, H. Oertel, T. Schenkel, Fluid–structure coupled cfd simulation of the left ventricular flow during filling phase, Biomed. Eng. A 8 (2005) 567–576.
[18] Y. Cho, S. Jun, S. Im, K. Hyun-Gyu, An improved interface element with variable nodes for non-matching finite element meshes, Comput. Methods Appl. Mech. Eng. 194 (2005) 3022–3046.
[19] J. Dennis, R. Schnabel, Numerical Methods for Unconstrained Optimization and Nonlinear Equations, SIAM, Prentice-Hall Inc., NJ, 1996.
[20] S. Deparis, M. Fernandez, L. Formaggia, Acceleration of a fixed point algorithm for fluid–structure interaction using transpiration conditions, ESAIM:M2AN 37 (2003) 601–616.
[21] W. Dettmer, D. Peri, A computational framework for fluid–structure interaction: finite element formulation and applications, Comput. Methods Appl. Mech. Eng. 195 (2006) 5754–5779.
[22] S. Eisenstat, H. Walker, Globally convergent inexact newton methods, SIAM J Opt. 4 (1994) 393–422.
[23] H. Elman, D. Kay, D.J. Silvester, A. Wathen, Efficient preconditioning of the linearized Navier–Stokes equations, J. Comput. Appl. Math. 128 (2001) 261–279.
[24] E. Fadlun, R. Verzicco, P. Orlandi, J. Mohd-Yusof, Combined immersed-boundary finite-difference methods for three-dimensional complex flow simulations, J Comput. Phys. 161 (2000) 35–60.
[25] C. Farhat, M. Lesoinne, P. LeTallec, Load and motion transfer algorithms for fluid/structure interaction problems with non-matching discrete interfaces: momentum and energy conservation, optimal discretization and application to aeroelasticity, Comput. Methods Appl. Mech. Eng. 157 (1998) 95–114.
[26] C. Farhat, M. Lesoinne, N. Maman, Explicit/implicit time integration of coupled aeroelastic problems: three-field formulation, geometric conservation and distributed solution, Int. J. Numer. Methods Fluids 21 (1994) 807–835.
[27] V. Girault, R. Blowinski, H. Lopez, J. Vila, A boundary multiplier/fictitious domain method for the steady incompressible Navier–Stokes equations, Numer. Math. 88 (2001) 75–103.
[28] V. Girault, P.A. Raviart, Finite Element Methods for the Navier–Stokes Equations, Springer-Verlag, 1986.
[29] R. Glowinski, T. Pan, J. Periaux, Numerical simulation of a multi-store separation phenomenon: a ficticious domain approach, Comput. Methods Appl. Mech. Eng. 195 (2006) 5566–5581.
[30] C. Greenshields, H. Weller, A unified formulation for continuum mechanics applied to fluid–structure interaction in flexible tubes, Int. J. Numer. Methods Eng. 64 (2005) 1575–1593.
[31] P. Gresho, Incompressible fluid dynamics: some fundamental formulation issues, Ann. Rev. Fluid Mech. 23 (1991) 413–453.
[32] P. Gresho, R. Sani, Incompressible flow and the finite element method I advection–diffusion, John Wiley and Sons, Ltd., 1998.
[33] P. Gresho, R. Sani, Incompressible flow and the finite element method II, isothermal laminar flow, John Wiley and Sons, Ltd., 1998.
[34] J. De Hart, G. Peters, P. Schreuers, F. Baaijens, A three-dimensional computational analysis of fluid–structure interaction in the aortic valve, J. Biomech. 36 (2003) 103–112.

[35] M. Heil, An efficient solver for the fully coupled solution of large-displacement fluid–structure interaction problems, Comput. Methods Appl. Mech. Eng. 43 (2008) 91–101.
[36] M. Heil, A. Hazel, J. Boyle, Solvers for large-displacement fluid–structure interaction problems: segregated versus monolithic approaches, Comput. Mech. 43 (2008) 91–101.
[37] M. Heinstein, T. Laursen, A three-dimensional surface-to-surface projection algorithm for non-coincident domains, Comput. Methods Appl. Mech. Eng. 69 (2003) 277–324.
[38] J. Coook, C. Hirt, A. Amsden, An arbitrary Lagrangian–Eulerian computing method for all flow speeds, J. Comput. Phys. 14 (1974) 227–253.
[39] J. Hron, M. Madlik, Fluid–structure interaction with applications in biomechanics, Nonlinear Anal. Real. World Appl. 8 (2007) 1431–1458.
[40] A. Huerta, L.K. Wing, Viscous flow with large free surface motion, Comput. Methods Appl. Mech. Eng. 69 (1988) 277–324.
[41] D. Kay, D. Loghin, A.J. Wathen, A preconditioner for the steady-state Navier–Stokes equations, SIAM J. Sci. Comput. 24 (2002) 237–256.
[42] O. Ladyzhenskaya, The Mathematical Theory of Viscous Incompressible Flow, Gordon and Breach, 1969.
[43] J. Lemmon, A. Yoganathan, Computational modeling of left heart diastolic function: examination of ventricular dysfunction, J. Elasticity 122 (2000) 297–303.
[44] H. Liu, S. Krishnan, S. Marella, H. Udaykumar, Sharp interface cartesian grid method. II: A technique for simulating droplet interactions with surfaces of arbitrary shape, J. Comput. Phys. 210 (2005) 32–54.
[45] LE. Malvern, Introduction to the Mechanics of Continuous Medium, Prentice-Hall, 1969.
[46] S. Marella, S. Krishnan, H. Liu, H. Udaykumar, Sharp interface cartesian grid method I: An easily implemented technique for 3d moving boundary computations, J. Comput. Phys. 210 (2005) 1–31.
[47] D. McQueen, C. Peskin, A 3d computational method for blood flow in the heart. II. Contractile fibers, J. Comput. Phys. 82 (1989) 289.
[48] D. McQueen, C. Peskin, A three-dimensional computer model of the human heart for studying cardiac fluid dynamics, Comput. Graph. 34 (2000) 56–60.
[49] G. McVittie, A systematic treatment of moving axes in hydrodynamics, Proc. Roy. Soc. London A 196 (1949) 285–300.
[50] M. Nash, Mechanics and Material Properties of the Heart using an Anatomically Accurate Mathematical Model, Ph.D. Thesis, University of Auckland, 1998.
[51] M. Nash, P. Hunter, Computational mechanics of the heart, J. Elasticity 61 (2000) 113–141.
[52] R. Nicolaides, Existence, uniqueness and approximation for generalized saddle point problems, SIAM J. Numer. Anal. 19 (1982) 349–357.
[53] F. Nobile, Numerical approximation of fluid–structure interaction problems with application to haemodynamics, Ph.D. Thesis, École Polytechnique Fédérale de Lausanne, 2001.
[54] D. Nordsletten, Fluid–Solid Coupling for the Simulation of Left Ventricular Mechanics, Ph.D. Thesis, University of Oxford, 2009.
[55] D. Nordsletten, P. Hunter, N. Smith, Conservative and non-conservative arbitrary Lagrangian–Eulerian forms for ventricular flows, Int. J. Numer. Methods Fluids 56 (2008) 1457–1463.
[56] D. Nordsletten, N. Smith, Triangulation of p-order parametric surfaces, J. Sci. Comput. 34 (2007) 308–335.
[57] D. Nordsletten, N. Smith, D. Kay, A non-conforming monolithic finite element method for problems of coupled mechanics: Linear analysis, SIAM J. Numer. Anal., in review.
[58] D. Nordsletten, N. Smith, D. Kay, A preconditioner for the finite element approximation to the ALE Navier–Stokes equations, SIAM J. Sci. Comput. 32 (2010) 521–543.
[59] K. Perktold, G. Rappitsch, Computer simulation of local blood flow and vessel mechanics in a compliant carotid artery bifurcation model, J. Biomech. 28 (1995) 845–856.
[60] A. Quarteroni, A. Valli, Numerical Approximation of Partial Differential Equations, Springer-Verlag, 1994.
[61] I. Ramiere, P. Angot, M. Belliard, A fictitious domain approach with spread interface for elliptic problems with general boundary conditions, Comput. Methods Appl. Mech. Eng. 29 (2007) 766–781.
[62] V. Shankar, H. Ide, Aeroelastic computations of flexible configurations, Comput. Struct. 30 (1988) 15–28.
[63] A. Slone, K. Pericleous, C. Bailey, M. Cross, C. Bennett, Aeroelastic computations of flexible configurations, Appl. Math. Model. 28 (2004) 211–239.
[64] R. Temam, Navier–Stokes Equations and Non-linear Functional Analysis, SIAM, 1983.
[65] R. Temam, Navier–Stokes Equations. Theory and Numerical Analysis, North-Holland, 1984.
[66] R. Unger, M. Haupt, P. Horst, Application of Lagrange multipliers for coupled problems in fluid and structural interactions, Comput. Struct. 85 (2007) 796–809.
[67] X. Wang, W. Liu, Extended immersed-boundary method using fem and rkpm, Comput. Methods Appl. Mech. Eng. 193 (2004) 1305–1321.
[68] Z. Warsi, Conservation form of the Navier–Stokes equations in general nonsteady coordinates, AIAA J. 19 (1980) 240–242.
[69] H. Watanabe et al, Multiphysics simulation of left ventricular filling dynamics using fluid–structure interaction finite element method, Biophys. J. 87 (2004) 2074–2085.
[70] A.J. Wathen, D. Loghin, D. Kay, H.C. Elman, D.J. Silvester. A new preconditioner for the Oseen equations. in: Proceedings of the European Conference on Numerical Mathematics and Advanced Applications, 2001.
[71] Y. Yang, H. Udaykumar, Sharp interface cartesian grid method. III: Solidification of pure materials and binary solutions, J. Comput. Phys. 210 (2005) 55–74.
[72] H. Zhang, R. Camarero, R. Kahawita, Conservation form of the equations of fluid dynamics in general nonsteady coordinates, AIAA J. 22 (1985) 1819–1822.